Cavity Beam Position Monitors State of the Art and Design Studies in the context of the ILC project

Author: Laura Karina Pedraza

External Supervisors:
Nuria Fuster
Daniel Esperante
Benito Gimeno

Local Supervisor:
Oxana Smirnova
Examiner:
Joakim Cederkäll

Academic year: 2023

Abstract

The aim of this master thesis project is the study and evaluation of the design of cavity beam position monitors (BPM) for the International Linear Collider (ILC) project. The state-of-the-art of BPMs is investigated to determine the most appropriate existing BPM design for the requirements of the ILC. The theoretical background on resonant cavities, including the beam coupling to the BPM, is examined. This knowledge enables the understanding of how certain parameters can affect the performance of the detector. To this end, a design investigation is carried out by analyzing the frequency spectrum of the beam for choosing the operational frequency of the resonator. Different common-mode-rejection methods are evaluated as well. Theoretical predictions are confirmed by 3D electromagnetic simulations, with the commercial software CST, based on a basic design of cavity BPM. The simulations are also performed in order to understand the impact of the cavity geometry on the BPM. The identification of the dipole mode signal for an offset beam corroborates the working principle of the cavity BPM. The particle-in-cell (PIC) solver from CST is revealed to be the most adequate for the simulation of the cavity BPM, allowing an efficient extraction of the dipole field induced by the beam. The state-of-the-art and the numerical results support the design of a cylindrical cavity with operational frequency of 1.495 GHz, with rectangular waveguides output ports used as filters to reject the monopole mode signal.

Acknowledgements

Contents

Nomenclature and acronyms

a radius of the cavity cylinder

c_0 speed of light in vacuum

f_{mnp} resonance frequency of an mnp mode

$f_{\mathbf{RF}}$ acceleration frequency of the RF cavities

$f_{\mathbf{rep}}$ repetition frequency of the macro bunches

J_m m-th Bessel function

j_{mn} n-th zero of the m-th Bessel function J_m

k_{mnp} wavenumber of an mnp mode

L length of the cavity cylinder

l_x, l_y dimensions of the rectangular waveguide

$P_{\mathbf{wall}}$ power dissipated in the cavity walls

$P_{\mathbf{out}}$ power dissipated out of the cavity

Q_0 internal or unloaded quality factor

$Q_{\mathbf{ext}}$ external quality factor

$Q_{\mathbf{L}}$ loaded quality factor

$q_{\mathbf{bunch}}$ bunch charge

(R/Q) normalized shunt impedance

T_r transit time factor

$t_{\mathbf{beam}}$ macro pulse length

$t_{\mathbf{bunch}}$ bunch spacing

$V_{b \rightarrow m}$ voltage induced from the beam to a mode

V_{mnp} voltage of the cavity mode mnp

$V_{\mathbf{out},mnp}$ output voltage of the cavity for the mode mnp

W_s energy stored in the cavity

δx, δy transverse offsets of the beam

τ time constant

ω_{mnp} angular resonance frequency of an mnp mode

σ standard deviation of the bunch on the time domain

σ_z bunch length

BPM beam position monitors

CM common-mode

EM electromagnetic

FT Fourier transform

FWHM full width half maximum

ILC International Linear Collider

IP interaction point

LHC Large Hadron Collider

PEC perfect electric conductive

PIC particle-in-cell

Q-value quality factor

RF radio frequency

TE transverse electric

TM transverse magnetic

UHV ultra-high vacuum

Introduction

The International Linear Collider (ILC) project considers two large (~ 20 km) linear accelerators intersecting at the interaction point (IP), where electrons and positrons collide at nearly the speed of light. The project's goal is to upgrade our knowledge on the basic constituents of matter and uncover fundamental questions on particle physics, such as the nature of dark matter and the existence of supersymmetry [ILC]. In order to achieve the collision at the IP, since the ILC beam's dimensions on the vertical direction are on the nm range, high-resolution beam position monitors (BPMs) are required. This device's task is to resolve, as accurately as possible, the position of the travelling beam on the transverse plane.

Traditional BPMs detect the beam's position by identifying the E-field generated by the charged particles at specific locations in the pipe. These detectors present some limitations on the resolution they are able to perform in the position reading (~ 1 μm). Resonant BPMs operate under the principle of detection of special field configurations (resonant modes) induced by an off-centered beam on a cavity. Because of the resonating behavior, these BPMs offer a higher position sensitivity, allowing to determine the beam's position with greater resolution (in the order of hundred nanometers), matching the ILC requirements [Lor98] [Nak08]. However, the proper-functioning of cavity BPMs (their ability to perform the measurement precisely and accurately) requires several considerations to be made during the design process.

Outline of the thesis

First, the state-of-the-art on beam position monitoring is presented on chapter 1. The operation modes of existing types of BPMs are briefly described such as button, split-plane and stripline BPMs. Further focus is given on resonant cavity BPMs. The different BPMs are then compared according to the ILC beam diagnosis requirements.

Due to the complexity of the cavity BPMs, chapter 2 is dedicated to the theory of the working principle. The expression of the output signal is derived by analyzing the eigenmodes existing on the cavity, the BPM parameters and the beam coupling to the cavity.

In chapter 3, design considerations for the ILC requirements are carried out. The operational frequency is evaluated by analyzing the frequency spectrum of the beam and by evaluating the cavity geometry. Additionally, some common-mode (CM) rejection methods are analyzed.

Finally, results of 3D electromagnetic simulations are presented on chapter 4 performed by using the commercial software CST Studio Suite. An eigenmode study allows the comparison of theoretical and simulated resonating modes in a specific cavity geometry. CST wakefield and PIC solvers were compared by analyzing the beam simulation results and the extraction of the resonating signal used to resolve the beam offset.

To conclude, the results are discussed as well as the future opportunities for further development of the project.

Chapter 1

State-of-the-Art of BPMs

BPMs are non-invasive electromagnetic *pick-ups* that can be used to derive the center of mass of the beam with respect to the center of the beam pipe. Generally, a BPM consists of a **BPM pick-up**, the electrodes that retrieve the electrical signal, and the **read-out electronics**, to process the signals and provide the beam position [Wen20].

1.1 Broadband BPMs

All broadband BPMs are considered to be non-resonating BPM pick-ups. This section aims to give a brief description of some of these BPMs and their working mechanisms. Advantages and disadvantages of these BPMs are described in greater detail in section 1.3.

1.1.1 Working principle and characteristics

For a basic BPM, one can retrieve the beam position in both transverse planes, by arranging 4 electrodes symmetrically around the vacuum pipe: horizontal and vertical electrodes allow to retrieve the position along the x and y axis, respectively. The goal of the measurement is to evaluate the charges induced by the E-field of the beam on the insulated plates. One will detect a uniform E-field in the case that the beam is perfectly centered on the pipe, and a non-uniform distributed field on the other case. The closer the beam is to one of the plates, the higher the image current will be. This is called the *proximity effect* [FKL08]: the current density depends on the distance of the beam with respect to the center of the pipe. In the horizontal direction
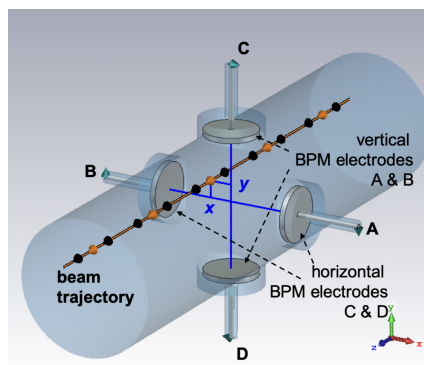

Figure 1.1: Scheme of a traditional BPM pick-up [Wen20].

one can extract the difference of voltage between plates A and B (figure 1.1) to retrieve the

horizontal offset of the beam (δx):

$$V_{\Delta,x} = V_A - V_B \propto I_{\text{beam}} \times \delta x$$

By normalizing by the sum of the signals $V_{\Sigma,x}$, it is possible to obtain the position information independently of the beam intensity I_{beam}: $V_{\Delta,x}/V_{\Sigma,x} \propto \delta x$. In particular, the horizontal position can be expressed as

$$\delta x = \frac{1}{s_x}\frac{V_{\Delta,x}}{V_{\Sigma,x}} + \epsilon_x$$

where s_x is the horizontal sensitivity and ϵ_x is the error in the horizontal direction [Wen20].

In general, each horizontal electrode retrieves a signal:

$$V_{\text{elec},x}(\delta x, \delta y, \omega) = s_x(\delta x, \delta y)Z(\omega)I_{\text{beam}}(\omega) \tag{1.1}$$

where Z is the transfer impedance, representing the transfer of beam current to voltage signal, which depends on the frequency ω of the beam. $s_x(\delta x, \delta y)$ is the sensitivity function in the horizontal direction, reflecting the coupling strength between the beam and the electrode, which depends on the transverse offsets of the beam (δx, δy).

The following characteristics are essential for the good-functioning of a BPM [FKL08] [Wen11]:

- **Integration time**: time during which the measurement is taken to resolve the beam position of a single bunch or all bunches, or the average over one or several pulses.

- **Position resolution**: the minimum beam displacement difference the BPM can statistically resolve.

- **Position sensitivity**: proportional constant $s_x(\delta x, \delta y)$ between the beam displacement δx or δy and the output signal. Yet, in some cases the sensitivity can depend on the position of the beam:

  - if s_x depends on δx one talks about **non-linearity** of the position sensitivity.
  - if s_x depends on δy one talks about **horizontal-vertical coupling** or **cross-coupling**.

  Both these cases limit the position resolution and can lead to inaccurate measurements. The same reasoning can be done for the vertical position sensitivity s_y in the case of vertical electrodes.

- **Accuracy**: ability of position reading relative to a fix-point such as the center of the beam pipe (influenced by cryogenic environments).

- **Dynamic range**: range of beam current or beam position to which the system can provide a valid measurement.

- **Reproducibility and long term stability**.

- **Signal-to-noise ratio**: ratio of desired signal to unwanted noise that limits the position resolution.

1.1.2 Button BPM

Button BPMs are the simplest type of BPM, and therefore are straightforward to understand. The device follows the working principle explained before with 4 symmetrically arranged buttons around the pipe. It is usual to rotate the position of the buttons around the pipe (as shown in
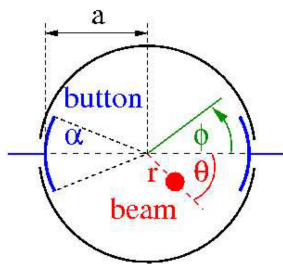
(a) Scheme of the BPM
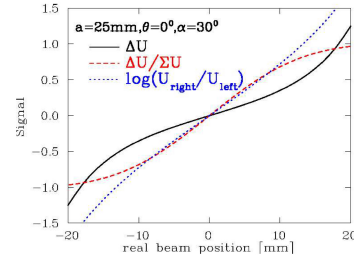
(b) Output signal as a function of the beam displacement

Figure 1.2: Button-type BPMs [FKL08].

figure 1.2) in order to avoid the synchrotron radiation emitted in the horizontal plane [Wen20]. However, this technique is prone to reduce the linear behavior of the detector.

For a rotation of $\alpha = 30$ degrees, the detector's signal shows a slightly linear behavior when it is normalized. The linearity can be improved by logarithmic amplification of the plate signals as shown in figure 1.2b. Another disadvantage of this BPM is the fact that the position sensitivity $s(\delta x, \delta y)$ depends on the frequency ω, which can lead to errors in the position reading.

1.1.3   Split-plane BPM

Split-plane BPMs are constituted by consecutive plates with a diagonal cut surrounding the beam (figure 1.3a). For these BPM, the signal strength is not obtained by proximity effect. As shown in figure 1.3b, the fraction of beam coverage on the electrodes gives a particular signal strength which allows one to derive the position. For instance, the voltage in the horizontal position V_x is proportional to the length of the beam projected on the electrode surface [FKL08].
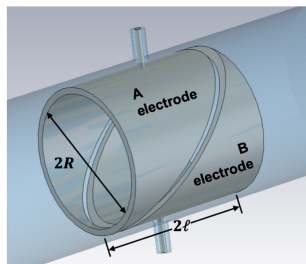
(a) Scheme the BPM
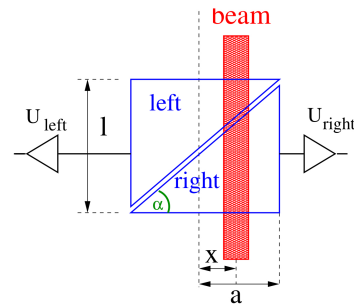
(b) Scheme of the working principle

Figure 1.3: Split-plane BPMs [Wen20] [FKL08].

The position sensitivity of this BPM is given by $s \sim 1/R$ where R is the radius of the detector, for a normalized signal. Very strong linearity and signal strength can be achieved with the inclusion of "guard rings" on the ground potential of the BPM. This prevents undesirable interaction between devices and circuits.

1.1.4   Stripline BPM

Stripline BPMs use long electrodes arranged around the beam allowing to distinguish between directions of propagation. Because of the length of the electrodes, this kind of BPM is suitable

for very short bunches [Wen20]. Since the length of the electrodes is known, one can compute the speed of the beam thanks to this BPM. For the previously considered BPMs, the effect of the signal propagation was not considered. This characteristic becomes more important when the size of the bunch is comparable to the size of the detector. It is also possible to distinguish beams propagating in opposite directions, which is particularly useful for synchrotron colliders.
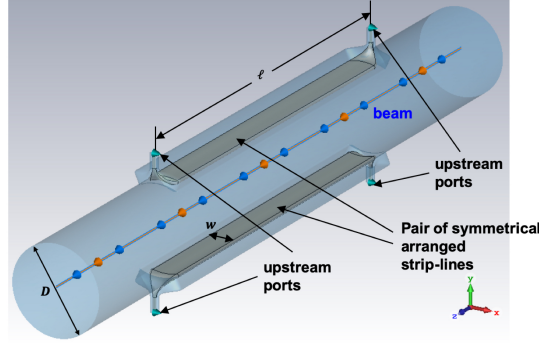
Figure 1.4: Scheme of a stripline BPM [Wen20].

As shown in figure 1.5, the upstream ports produce two counter-propagating signals when the beam passes. The two signals are produced on port 1 at $t = 0$. At $t = l/c_0$ (where l is the length of the electrodes), the beam reaches port 2, where one of the two counter-propagating signals produced is canceled because of a destructive interference with the first signal. Both signals propagating in the opposite direction as the beam are recorded at port 1, with a difference in timing that leads to the calculation of the speed of the beam. The length of the electrodes has to be chosen carefully to avoid the case in which the bunch repetition $t_{\text{bunch}} = 2l/c_0$. In this case the signal generated by the first bunch can be canceled by the signal generated by the second bunch, producing no net signal recorded [FKL08].
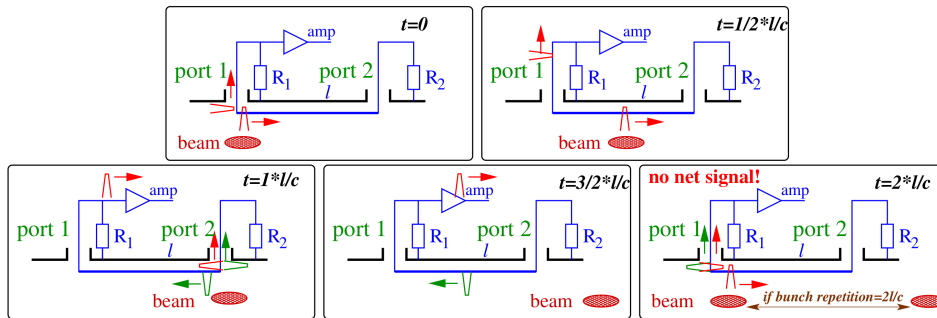
Figure 1.5: Working principle of a stripline BPM [FKL08].

1.2 Resonant BPMs

Resonant BPMs or cavity BPMs operate under the principle of measurement of special field configurations resonating at specific frequencies on a cavity. Indeed, the cavity constitutes a discontinuity along the pipe where stationary waves can be induced by the passage of the beam. The amplitude of these different resonating modes depends on the bunch charge (q_{bunch}), on the cavity orientation, and on the beam position δx or δy [Vit09]. In the context of this study, cylindrical or "pill-box" cavities are considered, but the mechanism is almost identical to the one of rectangular cavities.

1.2.1 Working principle

An infinite number of electromagnetic modes can resonate inside a perfect electric conductive (PEC) cavity [Gus22]. The short bunches of a beam can couple with the so-called transverse magnetic (TM) modes of the cavity (this is explained with more detail on chapter 2). In particular, two specific modes are of interest: TM_{010}, also called the *monopole*; and TM_{110}, the *dipole*. These modes are degenerate, which means that two different polarizations are generated. A schematic representation of these modes can be observed in figure 1.6a.
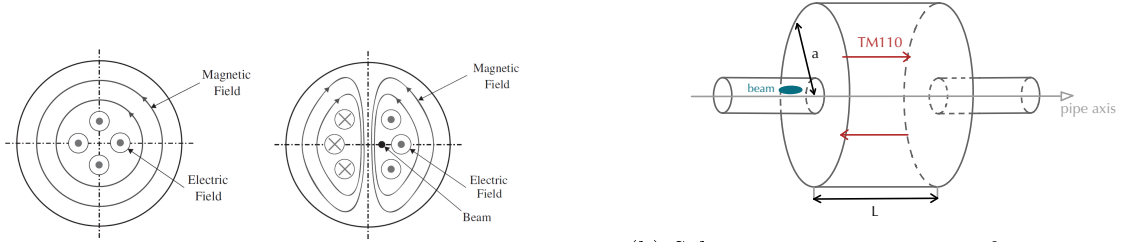
(a) Transverse view of the TM_{010} and TM_{110} modes

(b) Schematic representation of a cavity BPM with the E-field (in red) of the TM_{110} mode

Figure 1.6: Cylindrical cavity BPM [Vit09].

A beam completely centered will excite the monopole mode only, since the amplitude of the dipole is zero on the pipe axis. Therefore, an offset on the beam induces the dipole mode. In fact, the voltage induced by the dipole mode is proportional to the beam displacement (demonstration on chapter 2). In the horizontal case,

$$V_{TM110} \propto I_{\text{beam}} \times \delta x$$

As shown in figure 1.7, for the dipole mode, a beam with a greater offset (continuous line) generates a higher signal than a beam with a smaller offset (dashed line). Additionally, one will observe signals with opposite phases for offsets of the same magnitude but opposite sign (continuous and dotted lines), hence the importance of retrieving both amplitude and phase of the excited fields for the position reading.
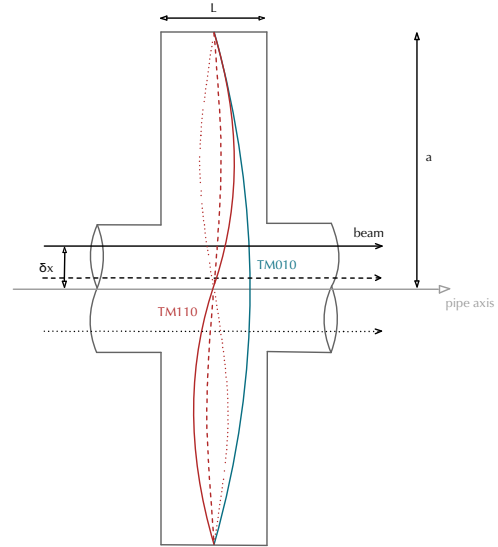
Figure 1.7: Schematic representation of the E-field induced for the monopole (blue) and dipole (red) in a cavity BPM [Vit09].

Essentially, to perform a beam position measurement in a cavity BPM, one has to consider the following:

- The magnitude of the dipole mode leads to the value of beam offset δx or δy.

- The sign of this offset can be reconstructed with the phase of the signal.

- The dipole mode has different polarizations. By differentiating them one can distinguish horizontal δx or vertical δy displacements.

The excited signals are extracted through coupling to an external circuit where amplitude of the different modes can be separated on the frequency domain.

1.2.2   Advantages

Cavity BPMs are well suited for two different scenarios: when high-resolution is required, since measurements up to the nm-range can be resolved, or when the beam current is very low, down to 1 nA. These applications are possible since these BPMs can achieve a very high impedance (kΩ) and high sensitivity. For the dipole mode, there is a strong linearity on the beam position over a wide dynamic range (several mm). The position resolution that can be achieved with a cavity BPM is in the nm range according to the literature [Nak08] [Hay19]

A mechanical advantage of this BPM is the ability to extract the measurement with a single output. Cavity BPMs also save longitudinal space since the length of the cavity is usually small (some cm).

1.2.3   Disadvantages

In order to reach the high resolution that a cavity BPM guarantees to achieve, there are some corrections needed on the basic design of the detector.

Noise components

As stated before, the output signal is evaluated in the frequency domain where one can perform a mode separation. However, the output signal does not contain only V_{TM110} revealing the position of the beam, but also the sum of many other signals that were induced on the cavity by the beam, or that occur in the extraction process. In particular, the output signal at the resonance frequency of the dipole mode f_{110}, can present the following noise components [SW10]:

$$V_{\mathrm{out}}(f_{110}) = V_{110}(\delta x) + V_{0n0} + V_{110}(\delta x') + V_{\mathrm{TN}}$$

where $V_{110}(\delta x)$ is the signal of interest yielding the beam position, V_{0n0} is the common-mode (CM) contamination, $V_{110}(\delta x')$ is the effect of the beam angle and V_{TN} is the thermal noise.

CM-contamination

Since the maximum amplitude of monopole modes TM_{0n0} is in the pipe axis (figure 1.7), the excited E-field of TM_{0n0} modes is higher in amplitude than the TM_{110} E-field. It is possible to observe monopole contamination: the monopole TM_{010} signal overlaps the dipole signal in the frequency domain as shown in figure 1.8a.

(a) Output signals in the frequency domain   (b) Cavity BPM with waveguides attached

Figure 1.8: CM-contamination in a cavity BPM [Lor98] [Wen+09].

Other monopoles such as TM_{020} can pollute the dipole signal as well if the resonance frequency f_{020} is close enough to f_{110}. In order to exclude the monopole signals, one can attach a waveguide capable of high-pass filtering the contamination as shown in figure 1.8b [Wen+09]. Methods of CM-rejection are explained with more detail on section 3.2.

Effect of the beam angle

A beam traversing the cavity with an angle $\delta x'$ induces an error on the position reading. According to [Lor98], for a mode with wavelength λ, and a cavity with radius a and length L, this offset error is estimated to be

$$\frac{\delta x}{\delta x'} = \frac{2244.5}{\sin(\pi L/\lambda)} \frac{L^3}{a^2 \lambda} \left[\frac{\text{m}}{\text{mrad}} \right]$$

Transient response

It is important that the energy induced on the cavity by a passing bunch vanishes before the arrival of the next bunch. Therefore, the energy on the cavity must not last longer than the bunch spacing. For the ILC case, this parameter corresponds to $t_{\text{bunch}} = 360$ ns. This can be achieved, by lowering the quality factor Q_0 of the cavity by using less conductive materials. However, low Q-value causes wider signals in the frequency domain and therefore leakage of the CM at f_{110} which limits the resolution [Wen06].

Cross-talk

To obtain the beam displacement δx and δy, one has to measure both polarizations of the dipole mode. However, coupling to a polarization to extract the offset value can affect the other polarization. This low isolation between both polarizations is called *cross-talk*. This is problematic since a beam displacement in only one direction can give a non-zero response in the other direction, and lead to reading errors [Wen06]. According to the literature, this can be solved by using two separate cavities to extract both measurements independently, or use a transformation matrix to solve it [Luo+10].

Wakefields and heat-load

One of the most troublesome issues with cavity BPMs is the increase of beam induced wakefields in the cavity. As shown in figure 1.9, the field of a charged bunch can remain captured in a pipe discontinuity. Higher modes excited by the beam trapped on the cavity may cause transverse and longitudinal kicks on the beam, affecting its dynamics. In particular, a trapped monopole can raise the temperature in the cryomodule. This issue generally imposes a large effect on the beam and affects the overall performance of the accelerator [Wen+09].
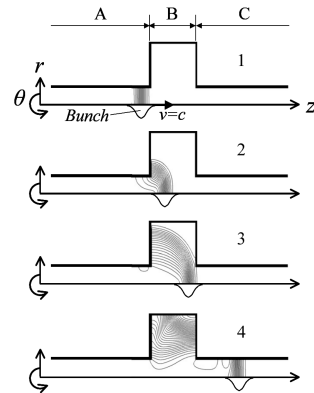
Figure 1.9: Wake fields induced by the passage of a bunch of charged particles [Fuj+07].

In addition to the previous considerations, one has to consider that the resonant frequency of the cavity is chosen to be different from the radio frequency (RF) accelerating frequency to avoid interferences. Furthermore, cavity BPMs usually cost a considerable amount of transverse space because the cavity radius is usually three times the pipe radius.

1.3 Best suitable BPM for the ILC

To accurately choose the most suitable BPM for the ILC requirements, it is relevant to first evaluate the design beam parameters and performance.

1.3.1 ILC characteristics and requirements

beam energy	2×250 GeV
luminosity	2×10^{34}
repetition frequency (f_{rep})	5 Hz
macro pulse length (t_{beam})	800 μs
bunch spacing (t_{bunch})	369 ns
bunch charge (q_{bunch})	3.2 nC
bunch length (σ_z)	300 μm
hor. beamsize (IP) (σ_x)	500 nm
vert. beamsize (IP) (σ_y)	5 nm

Figure 1.10: ILC beam parameters [Wen06].

The ILC beam is a bunched beam, separated into macro pulses that have a repetition frequency f_{rep} (figure 1.11). The accelerating RF superconducting cavities have a resonant frequency of 1.3 GHz. The radius of the beam pipe is 39 mm. The bunch sizes at the IP are specified in table 1.10. To achieve the design luminosity for the particle physics experiments, it is vital to preserve the low vertical emittance ε_y along the Main Linac. High resolution BPMs are therefore essential [Wen06].
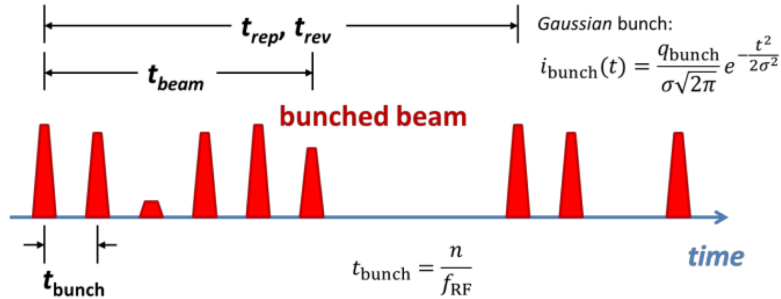
Figure 1.11: Structure of a bunched beam [Wen11].

Requirements for the ILC beam position monitoring can be divided into two types of requisites: measurement requirements and physical requirements.

Measurement requirements:

- Position resolution in the submicron range (< 1 μm) is required to preserve the vertical emittance [SW10].

- A position linearity of 2% is needed.

- The measurement has to be executed for single bunches, meaning that the measuring time has to be < 350 ns (inferior to t_{bunch}) so the signal in the cavity fades away in between bunches [Wen06].

- The dynamic range has to be large enough, so the detector can perform over a wide range of beam displacement (from 0 to $\pm$ 35 mm) and a full range of beam intensities as well (from 0 to 3.2 nC).

Physical requirements:

- The physical installation is limited to $\sim$ 200 mm of length (z direction) and $\sim$ 250 mm of diametric size in the transverse direction [Wen+09].

- The alignment error between the physical center of the BPM and the magnetic center of the quadrupoles must be < 200 μm.

- The detector needs to operate in ultra-high vacuum (UHV) and in a cryogenic environment (around 4 K), then the cool-down process has to be considered since it is prone to modify the Q-values because of the material shrinkage [Lor98].

- To prevent pollution of the neighboring RF cavities, cleanroom class 100 certification is necessary.

1.3.2   BPM Comparison

According to characteristics described previously for the different kinds of BPMs, table 1.1 describes advantages and disadvantages of the BPMs relative to the requirements of the ILC.

BPM type	Button	Split-plane	Stripline	Cavity
Coupling	Capacitive coupling to the beam E-field		EM coupling to the beam	Resonant
Resolution	Limited at 1 μm			< 1 μm (some nm [Nak08])
Facilities	Electron accelerators and proton linacs	Proton synchrotron with low frequencies	Synchrotron Colliders	Free-electron lasers and electron-positron colliders
Advantages	- Short bunches - Short installations - Simple mechanics	- Large signal amplitude - High linearity - Non H-V coupling	- Consideration of signal propagation - Short bunches - Distinguish counter-propagating beams	- Higher resolution - Short bunches - Low intensity beams
Disadvantages	- Non-linearities - H-V coupling	- Limited to bunches much longer than the BPM length - Hard mechanical realization	- Strong mechanical requirements - Cost longitudinal space	- Increment of wakefields - Cost transverse space

Table 1.1: Comparison table of existing BPMs according to ILC requirements. On red are characteristics that are not suitable for ILC and on green are requirements that are fulfilled.

The main characteristic that makes cavity BPM eligible for the position monitoring in the ILC is the position resolution. Despite the several considerations that have to be made for their proper functioning, cavity BPM are the only BPM shown to be able to reach some nm of resolution, essential to conserve the vertical emittance of the ILC beam.

Chapter 2

Cavity BPMs Theory

Proper design studies of a cavity BPM require deep understanding of the coupling of the beam with the resonator. The comprehension of the field configurations on the cavity, allows to choose a proper geometry producing a specific resonance frequency and to improve the signal extraction for an accurate position measurement. Resonant cavities are simply waveguides enclosed by two short-circuiting planes where boundary conditions have to be met. Allowed modes in the cavity oscillate between pure electric and pure magnetic energy [Lor98]. The field patterns that can exist inside a cavity can be:

- transverse magnetic (TM) modes (no longitudinal H-field component).

- transverse electric (TE) modes (no longitudinal E-field component).

TM modes are of interest since the E-field is longitudinal, following the beam direction. Their resonance frequency depends on the sizes on the geometry and can be analytically calculated in the case of simple geometries (such as rectangular or cylindrical).

2.1 Eigenmodes of a resonant cavity

The electromagnetic fields that can resonate in a cavity can be calculated from Maxwell equations in the frequency domain. The calculation of the resonant modes in a PEC cylindrical cavity can be found in the appendix section A. From this result (equation A.10), resonance frequency of an mnp mode (f_{mnp}) is found to be

$$f_{mnp} = \frac{c_0 k_{mnp}}{2\pi} \quad \text{where} \quad k_{mnp} = \sqrt{\left(\frac{j_{mn}}{a}\right)^2 + \left(\frac{p\pi}{L}\right)^2} \tag{2.1}$$

where k_{mnp} is the wavenumber of the mode, m,n,p are node numbers in r, ϕ, and z directions respectively, a is the radius of the cylinder, L is the length of the cavity, c_0 is the speed of light in vacuum and j_{mn} is the n-th zero of the m-th Bessel function (J_m) [Gus22]. The mode TM$_{010}$ is the monopole mode, which is usually used for accelerating charged particles in RF cavities or for normalization of the signal in the case of BPMs. The expression of the E-field along the z direction is (from equation A.8)

$$E_{z,010} = C_{010} J_0 \left(\frac{j_{01} r}{a}\right) e^{i\omega_{010} t} \tag{2.2}$$

The E-field of the dipole mode TM_{110}, which is used for position detection, can be expressed as

$$E_{z,110} = C_{110} J_1 \left(\frac{j_{11} r}{a} \right) \cos \phi e^{i \omega_{110} t} \tag{2.3}$$

where C_{mnp} is the amplitude and ω_{mnp} is the angular frequency of the TM_{mnp} mode [Vit09]. A transverse view of both fields can be seen in figure 1.6a.

2.2   Cavity BPM parameters

In order to derive the output voltage of the cavity, it is first important to define the following cavity-BPM parameters:

2.2.1   Quality factors

On a cavity BPM, one can define three different quality factors (Q-values) [Lor98]:

Internal or unloaded quality factor (Q_0)

It is the Q-value of the cavity itself: a dimensionless parameter describing how underdamped the oscillations of a resonator are. It depends on the wall material, and it is defined as

$$Q_{0,mnp} = \frac{\omega_{mnp} W_s}{P_{\text{wall}}} \tag{2.4}$$

where W_s is the energy stored in the cavity and P_{wall} is the power dissipated in the cavity walls.

External quality factor (Q_{ext})

It describes the strength of the cavity coupling to the output network. Similarly to Q_0,

$$Q_{\text{ext},mnp} = \frac{\omega_{mnp} W_s}{P_{\text{out}}} \tag{2.5}$$

where P_{out} is the power dissipated out of the cavity.

Loaded quality factor (Q_{L})

It considers the total dissipation power of the cavity and output network. It is defined as

$$Q_{\text{L},mnp} = \frac{\omega_{mnp} W_s}{P} \tag{2.6}$$

where $P = P_{\text{wall}} + P_{\text{out}}$
     One can find the relation

$$\frac{1}{Q_{\text{L}}} = \frac{1}{Q_0} + \frac{1}{Q_{\text{ext}}} \quad \text{or} \quad Q_{\text{L}} = \frac{Q_0}{1 + \beta} \tag{2.7}$$

where $\beta = Q_0/Q_{\text{ext}} = P_{\text{out}}/P_{\text{wall}}$ is the coupling strength representing how effectively energy can be extracted from the cavity. To improve β, high Q_0 and low Q_{ext} is necessary.

2.2.2 Time constants

Time constant (τ)

It can be shown that the stored energy in the cavity W_s decays exponentially [Nak08] with a time constant defined as

$$\tau = \frac{Q_L}{\omega_{mnp}} \tag{2.8}$$

Indeed, since the power dissipated in the cavity is defined as $P = -\frac{\mathrm{d}W_s}{\mathrm{d}t}$, by taking the definition of Q_L in equation 2.6, W_s satisfies a differential equation that is solved as

$$W_s = W_0 e^{-\frac{\omega_{mnp}}{Q_L}t}$$

where W_0 is the initial energy stored in the cavity.

Transit time factor (T_r)

Since the electric field excited in the cavity is a function of time (equations 2.2 and 2.3), there is a phase shift during the time that the beam passes through the cavity. The voltage induced in a cavity of length L is

$$V = \int_{-L/2}^{L/2} E_0 e^{i\omega_{mnp}t} \mathrm{d}z = T_r L E_0$$

where T_r is the representation of the effect of the phase transition during the passage of the beam [Vit09].

$$T_r = \frac{\sin(\omega_{mnp}L/2c_0)}{\omega_{mnp}L/2c_0} \tag{2.9}$$

2.2.3 Normalized shunt impedance

The shunt impedance R is a magnitude representing the accelerating efficiency for an RF cavity [Lor98].

$$R = \frac{|\int \mathbf{E}\mathrm{d}\mathbf{s}|^2}{P_{\mathrm{wall}}} \tag{2.10}$$

Usually, the normalized shunt impedance (R/Q) is used to evaluate the effect of the beam in the cavity.

$$\left[\frac{R}{Q_0}\right]_{mnp} = \frac{|\int \mathbf{E}\mathrm{d}\mathbf{s}|^2}{P_{\mathrm{wall}}} \frac{P_{\mathrm{wall}}}{\omega_{mnp}W_s} = \frac{|V_{mnp}|^2}{\omega_{mnp}W_s} \tag{2.11}$$

It depends only on the cavity geometry and not the conductive quality or the condition of the walls. The shunt impedance is however unique for every mode excited in the cavity. It can be shown that (R/Q) is proportional to $(\delta x)^2$ (the beam offset squared) for the dipole mode, and that (R/Q) it is constant for the monopole mode [Nak08].

TM$_{110}$ dipole mode

For calculating the normalized shunt impedance one needs to compute the voltage V_{mnp} and the stored energy in the cavity W_s for this mode. First, by using the expression of the E-field along

the z direction from equation 2.3, one can compute the voltage excited in the cavity when a beam passes with an offset δx:

$$V_{110}(\delta x) = \int_0^L E_{z,110}(r = \delta x, \phi = 0) \, \mathrm{d}z$$

$$= C_{110}J_1\left(\frac{j_{11}\delta x}{a}\right)\int_0^{L/c} e^{i\omega_{110}t}c \, \mathrm{d}t$$

$$= C_{110}J_1\left(\frac{j_{11}\delta x}{a}\right)\frac{c}{i\omega_{110}}\left[e^{i\frac{\omega_{10}L}{c}} - 1\right]$$

which leads to

$$V_{110}(\delta x) = C_{110}J_1\left(\frac{j_{11}\delta x}{a}\right)LT_r e^{i\frac{\omega_{110}L}{2c}} \tag{2.12}$$

Then, one can compute the stored energy in the cavity from the dipole mode:

$$W_{s,110} = \int_V \frac{1}{2}\varepsilon_0 \left|E_{z,110}\right|^2 dV$$

$$= \frac{1}{2}\varepsilon_0 C_{110}^2 \int_z \int_\phi \int_r \left|J_1\left(\frac{j_{11}r}{a}\right)\cos(\phi)\right|^2 rdrd\phi dz$$

$$= \frac{\pi}{2}\varepsilon_0 C_{110}^2 L \int_r \left|J_1\left(\frac{j_{11}r}{a}\right)\right|^2 rdr$$

Yet, Bessel functions are orthogonal:

$$\int_0^a J_k\left(j_{km}\frac{\rho}{a}\right) J_k\left(j_{kn}\frac{\rho}{a}\right)\rho d\rho = \frac{1}{2}a^2 J_{k+1}\left(j_{km}\right)^2 \delta_{mn}$$

and, since $J_2\left(j_{11}\right)^2 = J_0\left(j_{11}\right)^2$ [Wol], the stored energy in the cavity is

$$W_{s,110} = \frac{\pi}{4}\varepsilon_0 C_{110}^2 a^2 L J_0\left(j_{11}\right)^2 \tag{2.13}$$

Recalling the definition of the normalized shunt impedance in equation 2.11 and using equations 2.12 and 2.13, one can derive

$$\left[\frac{R}{Q}\right]_{110} = \frac{4J_1\left(\frac{j_{11}\delta x}{a}\right)^2 LT_r^2}{\omega_{110}\pi\varepsilon_0 a^2 J_0\left(j_{11}\right)^2}$$

however, since $J_n(x) \simeq \frac{1}{n!}\left(\frac{x}{2}\right)^n$ for $x \approx 0$ [Wol], for the Bessel function J_1 one can approximate $J_1(\frac{j_{11}\delta x}{a}) \simeq \frac{j_{11}\delta x}{2a}$. This leads to

$$\left[\frac{R}{Q}\right]_{110} \simeq \frac{2\left(j_{11}\delta x\right)^2 LT_r^2}{\omega_{110}\pi\varepsilon_0 a^4 J_0\left(j_{11}\right)^2} \tag{2.14}$$

and thus, $[R/Q]_{110} \propto (\delta x)^2$ for δx small enough.

TM$_{010}$ monopole mode

Similarly, one can derive for the monopole mode the voltage excited in the cavity from equation 2.2

$$V_{010}(\delta x) = \int_0^L E_{z,010}(r = \delta x, \phi = 0) \, \mathrm{d}z = C_{010}J_0\left(\frac{j_{01}\delta x}{a}\right)LT_r e^{i\frac{\omega_{010}L}{2c}} \tag{2.15}$$

the energy stored in the cavity for the monopole mode

$$W_{s,010} = \int_V \frac{1}{2}\varepsilon_0 |E_{z,010}|^2 \ \mathrm{d}V = \frac{\pi}{2}\varepsilon C_{010}^2 a^2 L J_1 (j_{01})^2 \qquad (2.16)$$

and then, the normalized shunt impedance is

$$\left[\frac{R}{Q}\right]_{010} = \frac{2J_0 \left(\frac{j_{01}\delta x}{a}\right)^2 L T_r^2}{\omega_{010}\pi\varepsilon_0 a^2 J_1 (j_{01})^2} \simeq \frac{2L T_r^2}{\omega_{010}\pi\varepsilon_0 a^2 J_1 (j_{01})^2} \qquad (2.17)$$

Since the Bessel function J_0 can be approximated to a constant, according to $J_n(x) \simeq \frac{1}{n!}\left(\frac{x}{2}\right)^n$ for $x \approx 0$, it leads to $[R/Q]_{010} \sim$ constant for δx small enough.

2.3 Beam coupling to the cavity

2.3.1 Fundamental theorem of beam loading

A charge travelling through a beam pipe induces a *mirror charge* in the pipe. When the charge passes through a cavity, short bunches can excite an infinite number of stationary electromagnetic modes [Vit09]. A key element to derive the expression of the output voltage (for each mode) is the *fundamental theorem of beam loading*. It states that "the voltage induced by a charge travelling through a cavity is twice the effective voltage *seen* by the charge itself". The aim of the following section (taken from [Nak08]) is to provide a demonstration of this theorem.

Let's consider a cavity (with no energy loss) where initially there is no E-field, where a bunch of charge q passes through. The bunch excites $\mathbf{V}_{\mathrm{exc}}$ and then feels $\mathbf{V}_{\mathrm{eff}}$ (called the wakefield) which will cause a deceleration on it. In order to relate $\mathbf{V}_{\mathrm{exc}}$ and $\mathbf{V}_{\mathrm{eff}}$, one can define A and ε as the ratio and the phase shift between them respectively.

$$\mathbf{V}_{\mathrm{exc}} = - V_{b\to m}e^{i\varepsilon}$$
$$\mathbf{V}_{\mathrm{eff}} = - A\ V_{b\to m}$$

$V_{b\to m}$ is the voltage induced from the beam to a mode. The minus sign represents the effect of deceleration the bunch experiences.

When one considers the passage of a second bunch (with a phase transition of θ with respect to the first bunch), this one will feel the wakefield of the first bunch and its own excited field. Considering this, one can evaluate the field bunches 1 and 2 experience:

$$\mathbf{V_1} = \mathbf{V}_{\mathrm{exc}}$$
$$\mathbf{V_2} = \mathbf{V}_{\mathrm{eff}} + \mathbf{V}_{\mathrm{exc}}e^{i\theta}$$

It is pertinent to compute the acquired energy of two bunches ΔW_{beam} and the energy stored in the cavity $\Delta W_{\mathrm{cavity}}$ as well. The first one can be computed by taking the real part of the field both bunches experience:

$$\Delta W_{\mathrm{beam}} = q\,\mathrm{Re}\,(\mathbf{V_1}) + q\,\mathrm{Re}\,(\mathbf{V_2}) = -2qAV_{b\to m} - qV_{b\to m}\cos(\theta + \varepsilon)$$

And $\Delta W_{\mathrm{cavity}}$ can be calculated by taking the voltage in the cavity, which is the addition of the voltage excited by both bunches: $\mathbf{V}_{\mathrm{cavity}} = \mathbf{V}_{\mathrm{exc}}\,e^{i\theta} + \mathbf{V}_{\mathrm{exc}}$. Thus, the stored energy in the cavity can be computed by using the definition of (R/Q) (equation 2.11):

$$\Delta W_{\mathrm{cavity}} = \frac{|\mathbf{V}_{\mathrm{cavity}}|^2}{\omega(R/Q)} = \frac{\left|\mathbf{V}_{\mathrm{exc}}e^{i\epsilon}\left(e^{i\theta} + 1\right)\right|^2}{\omega(R/Q)} = \frac{2V_{b\to m}^2(1 + \cos\theta)}{\omega(R/Q)}$$

By conservation of energy

$$\Delta W_{\text{cavity}} = \Delta W_{\text{beam}} \Leftrightarrow \frac{2V_{b\to m}^2(1+\cos\theta)}{\omega(R/Q)} = 2qAV_{b\to m} + qV_{b\to m}\cos(\theta+\varepsilon)$$

Since θ varies arbitrarily, the previous equation leads to the system:

$$\begin{cases} qV_{b\to m}\sin\varepsilon = 0 \\ \frac{2V_{b\to m}^2}{\omega(R/Q)} - qV_{b\to m}\cos\varepsilon = 0 \\ \frac{2V_{b\to m}^2}{\omega(R/Q)} - 2qAV_{b\to m} = 0 \end{cases} \Leftrightarrow \begin{cases} \varepsilon = 0 \\ V_{b\to m} = \frac{\omega}{2}\left(\frac{R}{Q}\right)q \\ A = \frac{1}{2} \end{cases}$$

Therefore, $\mathbf{V}_{\text{exc}} = -V_{b\to m}$ and $\mathbf{V}_{\text{eff}} = -\frac{1}{2}V_{b\to m}$; there is no phase shift between $\mathbf{V}_{\text{exc}}$ and $\mathbf{V}_{\text{eff}}$ and the ratio between them is $1/2$, which provides the proof of the *fundamental theorem of beam loading*.

2.3.2   Voltage of a resonant mode excited by the beam

The theorem stated before also provides an expression of voltage of a resonant mode in the cavity excited by a passing beam

$$V_{b\to m} = \frac{\omega}{2}\left(\frac{R}{Q}\right)q \tag{2.18}$$

The demonstration does not consider the effect of the bunch length σ_z. Since it is not infitely small, the entirety of the bunch does not travel through the cavity at the same time. This provokes a phase shift during the passage which is $\omega z/c_0$. Considering a gaussian distribution of the bunch in the beam direction:

$$\frac{1}{\sqrt{2\pi}\sigma_z}\exp\left(-\frac{z^2}{2\sigma_z^2}\right)$$

By integrating the gaussian distribution representing all the particles in the bunch, the total voltage induced in the cavity can be deduced

$$V_{\text{total},b\to m} = \int_{-\infty}^{\infty} V_{b\to m}\frac{1}{\sqrt{2\pi}\sigma_z}\exp\left(-\frac{z^2}{2\sigma_z^2}\right)\exp\left(i\frac{\omega z}{c_0}\right)\mathrm{d}z = V_{b\to m}\exp\left(-\frac{\omega^2\sigma_z^2}{2c_0^2}\right)$$

Thus by using equation 2.18, the total voltage of a resonant mode mnp in the cavity excited by a passing beam is

$$V_{\text{total},b\to m} = \frac{\omega_{mnp}}{2}\left(\frac{R}{Q}\right)_{mnp} q\exp\left(-\frac{\omega_{mnp}^2\sigma_z^2}{2c_0^2}\right) \tag{2.19}$$

Then, if the bunch is not infinitely small, the excited voltage is reduced by the factor $\exp\left(-\frac{\omega^2\sigma_z^2}{2c_0^2}\right)$.

2.4   Output signals

2.4.1   Output voltage

The expression in equation 2.19 shows that the voltage induced from the beam to the cavity depends on the mode since the normalized shunt impedance (R/Q) is proper to each mode. The

energy stored in the cavity after passage of the beam can be derived from the definition of (R/Q) from equation 2.11 [Vit09]

$$W_s = \frac{V_{\text{total},b\to m}^2}{\omega_{mnp}(R/Q)_{mnp}} = \frac{\omega_{mnp}}{4}\left(\frac{R}{Q}\right)_{mnp} q^2 \exp\left(-\frac{\omega_{mnp}^2\sigma_z^2}{c_0^2}\right) \tag{2.20}$$

The output power can then be obtained from the definition of Q_{ext} (equation 2.5)

$$P_{\text{out}} = \frac{\omega_{mnp}W_s}{Q_{\text{ext}}} = \frac{\omega_{mnp}^2 q^2}{4}\frac{1}{Q_{\text{ext}}}\left(\frac{R}{Q}\right)_{mnp}\exp\left(-\frac{\omega_{mnp}^2\sigma_z^2}{c_0^2}\right) \tag{2.21}$$

And finally, the amplitude of the output voltage of the cavity for the mode mnp in the readout electronics with impedance Z is defined as

$$V_{\text{out},0} = \sqrt{ZP_{\text{out}}} = \frac{\omega_{mnp}q}{2}\sqrt{\frac{Z}{Q_{\text{ext}}}\left(\frac{R}{Q}\right)_{mnp}}\exp\left(-\frac{\omega_{mnp}^2\sigma_z^2}{2c_0^2}\right) \tag{2.22}$$

Because of the expression of the normalized shunt impedances for both monopole and dipole modes, in equations 2.17 and 2.14, where $[R/Q]_{110} \propto (\delta x)^2$ and $[R/Q]_{010} \sim$ constant, it is then proven that

$$V_{\text{out},110} \propto \delta x \quad \text{and} \quad V_{\text{out},010} \sim \text{constant}$$

Since the recovered signal out of the cavity oscillates with the frequency of the mode ω_{mnp} and decays exponentially with decay constant τ [Nak08], one will have at the output

$$V_{\text{out}}(t) = V_{\text{out},0}\sin(\omega_{mnp}t + \varphi)\exp\left(-\frac{t}{2\tau}\right) \tag{2.23}$$

2.4.2 Coupling to external circuits

To retrieve the output signal from a cavity one can implement different methods so the EM field couples with the exterior.
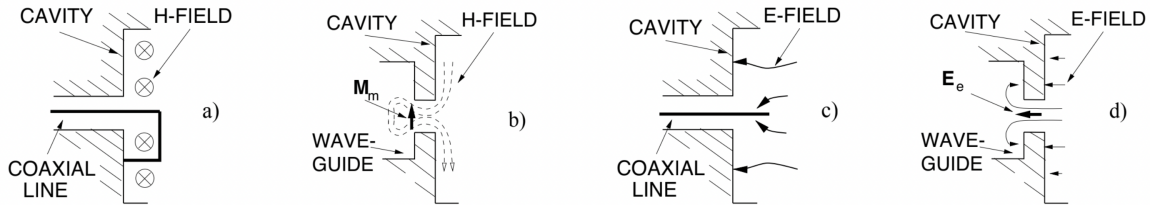
Figure 2.1: Schematic representation of the different magnetic and electric couplings to the exterior of the cavity [Lor98].

Schemes a) and b) from figure 2.1 show a magnetic coupling where the H-field can induce a voltage by passing through a loop for a) and where the H-field penetrates through a hole to an external waveguide for b). Electric couplings are shown in c) and d). The E-field can cause a current on a dipole (coaxial line) for c) or can induce a voltage through a hole for d) (similarly as b)). By choosing the right length of the antennas or its position, the coupling strength β can be improved. For the actual study, coupling mostly through holes are considered.

Chapter 3

Design Investigation of the Cavity BPM

This section's goal is the evaluation of the influence of parameters such as resonance frequency and geometry on the cavity's design and performance. First, in order to understand the choice of the operational frequency of the cavity, the ILC beam-type frequency spectrum is simulated. Then, the most recurring CM-rejection methods are described.

3.1 ILC frequency spectrum

3.1.1 ILC beam simulation

Table 1.10 summarizes the main ILC beam parameters. The described bunched beam has a bunch length $\sigma_z = 300$ μm. Thus, the standard deviation of a bunch in the time domain is $\sigma = \sigma_z/c_0$, considering the beam travels at c_0. The spacing between the bunches is $t_{\text{bunch}} = 369$ ns. The number of bunches in a macro-pulse is $n = t_{\text{bunch}} \times f_{\text{RF}} \sim 480$ bunches, where $f_{\text{RF}} = 1.3$ GHz is the frequency of the RF cavities [Wen06]. Therefore, the duration of a macro-pulse is $t_{\text{beam}} = n \times t_{\text{bunch}} \sim 177$ μs. Finally, the beam is separated into macro-bunches with a repetition frequency f_{rep} of 5 Hz, which makes $t_{\text{rep}} = 0.2$ s.

A Python code was developed to simulate the beam signal (B.1). Because of the difference in order of magnitude of the parameters, the easiest way to simulate the bunched beam is by performing a convolution of the Gaussian pulse over a Dirac comb: a periodic impulse function with the corresponding spacing t_{bunch}. Then, the obtained signal can be multiplied by a squared signal defining the length of the macro-pulses and the spacing between them.
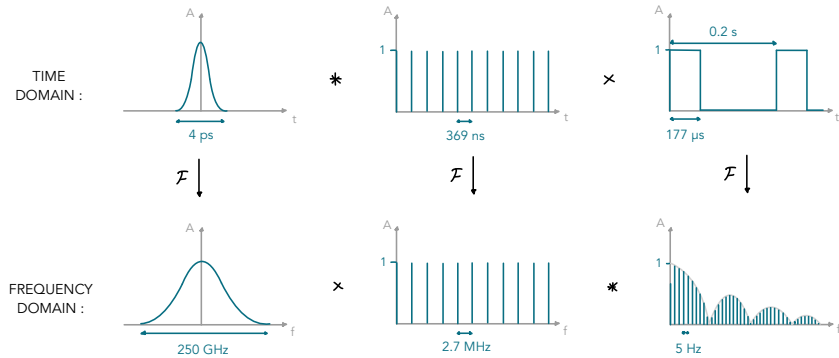

Figure 3.1: ILC bunched beam simulation technique and Fourier transform.

As showed in figure 3.1, the Fourier transform (FT) of the bunched beam can then easily

be simulated by using the FT properties. When going from the time domain to the frequency domain, a convolution becomes a multiplication and vice versa.

In the time domain, the Gaussian bunch is simulated as

$$i_{\text{bunch}}(t) = \frac{q_{\text{bunch}}}{\sigma\sqrt{2\pi}} e^{-\frac{t^2}{2\sigma^2}} \tag{3.1}$$

where σ is the standard deviation of the bunch in the time domain.

The Dirac comb (the impulse train) is simply defined as a function C_T, returning 1 whenever there is a bunch (every multiple of $T = t_{\text{bunch}}$) and 0 otherwise.

$$C_T(t) = \sum_{n=-\infty}^{\infty} \delta(t - nT) \tag{3.2}$$

Similarly, the rectangular pulse returns 1 inside a macro-pulse and 0 in the spacing between macro-pulses.

$$R(t) = \begin{cases} 1 & \text{if } (k \times t_{\text{rep}}) < t < (k \times t_{\text{rep}} + t_{\text{beam}}) \\ 0 & \text{otherwise} \end{cases} k \in \mathbb{N} \tag{3.3}$$

Those three elements of the beam were computed on Python as shown in figure 3.2.

(a) Gaussian bunch   (b) Dirac comb   (c) Rectangular pulse
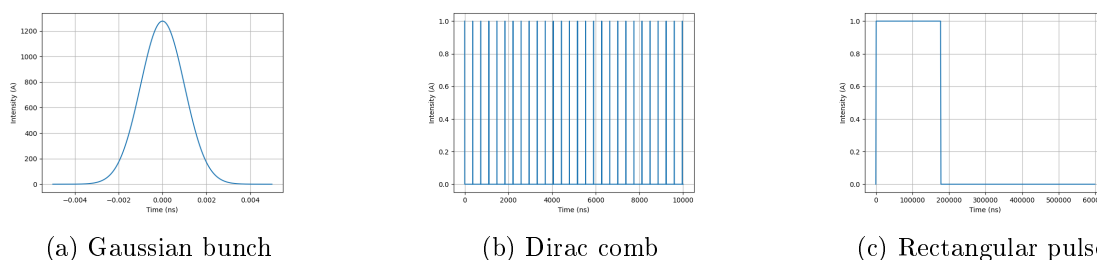
Figure 3.2: Decomposition of the ILC beam signal in the time domain simulated with Python.

3.1.2 Fourier Transform of the beam signal

In order to obtain the frequency spectrum of the beam, a FT can be implemented. The FT $\mathscr{F}$ of a function $f(t)$ can be defined as

$$\mathscr{F}\{f(t)\} = \int_{-\infty}^{\infty} f(t)e^{-2\pi i f t} dt \tag{3.4}$$

As shown in figure 3.1, due to the FT properties, on can compute separately the different components of the beam signal and then perform a multiplication and a convolution to reconstruct the entirety of the signal.

First, the FT of a Gaussian pulse is simply another Gaussian pulse. It can be shown that

$$\mathscr{F}\{i_{\text{bunch}}(t)\} = q \cdot e^{-2\sigma^2\pi^2 f^2} \tag{3.5}$$

Thus, the FT of the Gaussian bunch, is another Gaussian bunch with standard deviation $1/(2\pi\sigma)$ (figure 3.3a).

The FT of the Dirac comb can be computed as

$$\mathscr{F}\left\{C_T(t)\right\} = \frac{1}{T}C_{1/T}(f) = \frac{1}{T}\sum_{n=-\infty}^{\infty}\delta\left(f - \frac{n}{T}\right) \tag{3.6}$$

which represents another Dirac comb of period $1/T = 1/t_{\mathrm{bunch}}$.

The FT of a rectangular pulse with height A, rectangle length $k = 177$ μs and a period $T = 0.2$ s gives a Fourier series. According to the synthesis equation, any periodic function g can be reconstructed from cosine and sine waves as

$$g(t) = a_0 + \sum_{n=1}^{\infty}a_n\cos(2\pi ftn) - \sum_{n=1}^{\infty}b_n\sin(2\pi ftn) \tag{3.7}$$

where frequencies are multiples of the fundamental frequency f. According to [Smi+97], the Fourier series of the rectangular pulse is a frequency spectrum consisting of harmonics every f_{rep}, with

$$a_0 = Ad, \quad a_n = \frac{2A}{n\pi}, \quad b_n = 0 \tag{3.8}$$

where a_n and b_n coefficients are the real and imaginary part of the frequency spectrum on the synthesis equation, and where $d = k/T$.

(a) Gaussian bunch   (b) Dirac comb   (c) Rectangular pulse
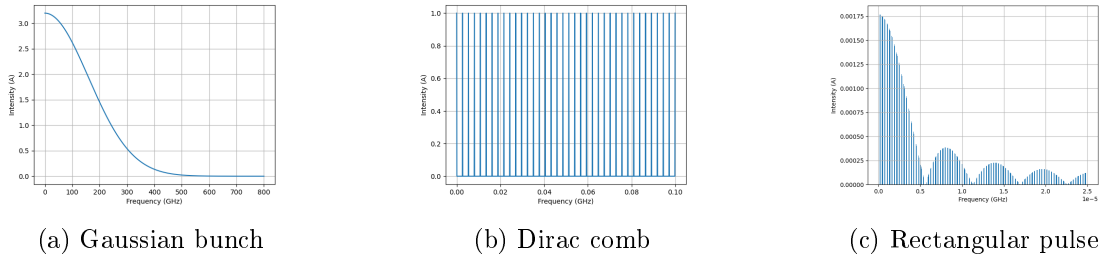
Figure 3.3: FT of the decomposed ILC beam signal on the frequency domain simulated with Python.

As explained by figure 3.1, by convolution of the FT of the Dirac comb with the FT of the rectangular pulse, and by multiplying that result with the FT of the Gaussian bunch, one can reconstruct the FT of the ILC beam signal by means of a developped Python code.

The obtained result is a Gaussian pulse with FWHM = 376 GHz, filled with harmonics repeated every 2.7 MHz (figure 3.4). It is noted that the operational frequency of the cavity BPM should be contained inside this spectrum. This does not represent an important limitation on this case since the spectrum is broad. For other beam signals, such as the Large Hadron Collider (LHC), where the frequency spectrum is extended up to 3 GHz, since the bunch length is bigger ($\sigma_{\mathrm{LHC}} = 1.3$ ns) [BC03], this has to be taken in consideration.

Figure 3.4: Frequency spectrum of the ILC beam signal with Python.

According to literature, cavity BPMs usually have an operational frequency of about 1-2 GHz [Hay15] [SW10]. The operational frequency can be chosen by modifying the dimensions of the cavity itself as shown in quation 2.1. The main limitation when choosing the resonance frequency of the cavity is the available physical space to place the detector. Moreover, the 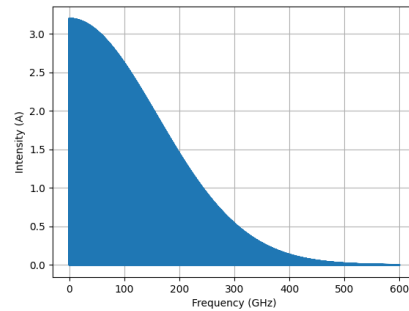monopole and dipole frequencies of the cavity BPMs are chosen to be separated symmetrically from the acceleration frequency: $f_{\mathrm{RF}} = 1.3$ GHz in the case of ILC. This means that f_{RF} is in the middle of f_{010} and f_{110}. A cavity with $L = 15$ mm and $a = 113$ mm give resonance frequencies of approximately $f_{010} = 1.01$ GHz and $f_{110} = 1.62$ GHz, which are well situated on the frequency spectrum of the beam.

3.2 CM-rejection methods

In practice, the material of the cavity walls is not PEC, which leads to a finite dissipation of energy into the cavity walls (Joule effect). For this reason, one will obtain a broad spectrum of frequencies when retrieving the signal out of the BPM. In addition, there is a strong excitation of the monopole mode, as explained in section 1.2, the signal of the monopole TM_{010} can overlap with the signal of interest (the dipole TM_{110}) in the frequency domain. In order to account for these effects and improve the accuracy of the position reading, rejection methods of the CM (monopole mode) are implemented. Since the dipole mode generates a field transverse to the z-axis, it can have a strong coupling with a properly designed waveguide. This waveguide acts then as a filter, removing the CM.

3.2.1 Cavity coupling to the waveguide

The field inside the cavity can couple to the attached waveguides (figure 1.8b) by passing through a rectangular slot. The modes from the cylindrical cavity can couple magnetically to the TE_{01} and TE_{10} modes of the rectangular waveguide (which corresponds to case b in figure 2.1, presented on the theory section). Yet, this is only possible when the magnetic field of the modes is parallel to the slot direction. One can use this property to read only the desired modes in the desired direction, as the ports to extract the signals are situated inside the waveguides [Nak08].

(a) TM$_{010}$ mode   (b) TM$_{110}$ mode (horizontal)   (c) TM$_{110}$ mode (vertical)
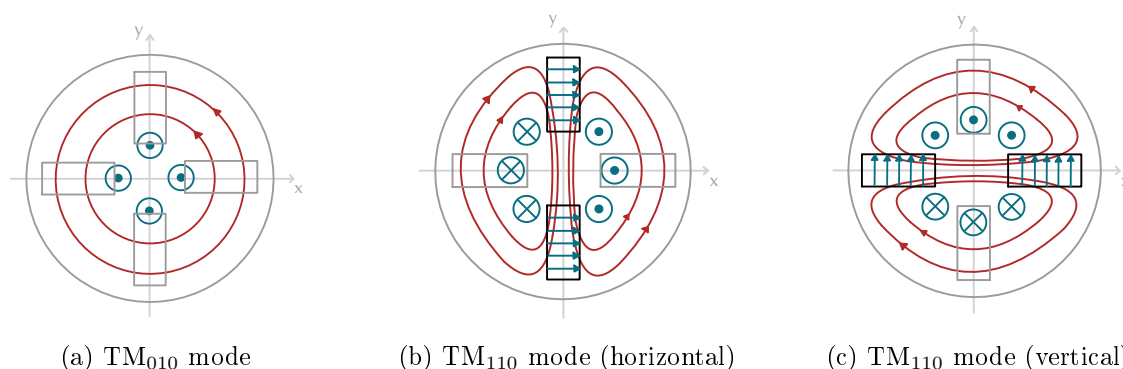
Figure 3.5: Schematic representation of the cavity modes coupling with the waveguide slot.

Four symmetrically arranged rectangular waveguides can be used for extracting the dipole signals, rejecting the monopole signal. As the magnetic field of the monopole mode is always perpendicular to the slot direction, it will never couple successfully to the waveguide, leading to a proper CM-rejection. The slots arranged vertically only couple with the horizontal polarization of the dipole mode, allowing one to read the beam position along the x-axis. Similarly, the slots

arranged horizontally grant beam position along the y-axis. Two waveguides per direction are necessary in order to keep the BPM symmetry, reducing the x-y coupling [Li+03].

3.2.2 Cut-off frequency of the waveguide

On top of the selective magnetic coupling, the waveguide can act as a very efficient high-pass filter. Indeed, every mode on the waveguide has a cut-off frequency that can be computed as

$$f_c = \frac{c_0 k_{t,mn}}{2\pi} \quad \text{where} \quad k_{t,mn} = \sqrt{\left(\frac{m\pi}{l_x}\right)^2 + \left(\frac{n\pi}{l_y}\right)^2} \tag{3.9}$$

where l_x and l_y are the horizontal and vertical dimensions of the rectangular waveguide [Gus22]. For TE modes, one can have $m = 0$ or $n = 0$ but not both $m = n = 0$ at the same time.

In the following, the example of the horizontal polarization of TM_{110} is presented. That polarization will couple to the fundamental mode of a waveguide with $l_x < l_y$ (figure 3.5b), the TE_{01} mode. The cut-off frequency of this mode in the waveguide is then calculated as

$$k_{t,01} = \frac{\pi}{l_y} \quad \Rightarrow \quad f_{c,01} = \frac{c_0}{2l_y} \tag{3.10}$$

One can choose the height of the waveguide l_y so that the cut-off frequency is higher than the monopole mode frequency and lower than the dipole mode frequency. This way the waveguide acts as a high-pass filter.

$$f_{010} < f_{c,01} = \frac{c_0}{2l_y} < f_{110} \tag{3.11}$$

For example, a waveguide height of $l_y = 122$ mm, the cut-off frequency of the TE_{01} mode is well included between the monopole and dipole cavity frequencies.

$$f_{010} = 1.01 < f_{c,01} = \frac{c_0}{2l_y} = 1.23 < f_{110} = 1.62 \text{ GHz} \tag{3.12}$$

These methods were successfully implemented and showed a proper CM-rejection, improving the performance of the cavity BPM in [Wen11] [Wen+09].

Chapter 4

3D-EM Simulations on CST Studio Suite

CST Studio Suite is an efficient 3D electromagnetic (EM) analysis software used for the design and optimization of EM systems [Glo]. By using this commercial software, one can evaluate the working principle of a regular cavity and then simulate the cavity BPM performance. In this study, CST parametric simulations have been performed to evaluate the impact of the cavity BPM geometry on its operation mode and its performance.

4.1 Eigenmode study

An eigenmode study is initially implemented in order to observe the allowed modes on a resonating cavity, according to its geometry. The beam is therefore not simulated in this study. Results obtained with the *eigenmode solver* on CST are then compared to theoretical predictions. Additionally, this study allowed as well the computation of the detector's dynamic range and the behavior of the shunt impedance R/Q.

Dimensions of the cylindrical cavity are chosen to be $a = 113$ mm and $L = 15$ mm as suggested by [Wen+09] [SW10] and [Wen06].

4.1.1 Resonance frequencies of monopole and dipole modes

Cavity geometry

Resonant frequencies of the different TM modes can be analytically calculated by means of equation 2.1. A MATLAB code (C.1), calculating j_{mn} the n-th zero of the m-th Bessel function J_m, was developed to compute the 6 lowest resonance frequencies of the mentioned geometry.

Mode	TM_{010}	TM_{110}	TM_{210}	TM_{020}	TM_{310}
f_{mnp}(GHz)	1.0161	1.6190	2.1700	2.3324	2.6958
Type	Monopole	Dipole	Quadrupole	Monopole	Sextupole

Table 4.1: TM modes resonance frequencies for a cavity with $a = 113$ mm and $L = 15$ mm computed with MATLAB.

With this geometry, frequencies of the first monopole and first dipole are well separated from the following frequencies. This will avoid having more noise components on the output signal.

The eigenmode solver in CST requires the definition of the geometry, the material and some boundary conditions [Com19b]. The material of the cavity is chosen as vacuum and its boundaries are PEC. For the boundary conditions one can define electric or magnetic walls, where the electric and magnetic transverse fields are equal to zero. The walls can be defined at:

The boundaries: electric wall ($E_t = 0$) (in green in figure 4.1) for all boundaries, since the structure is embedded in PEC material.

The symmetry planes:

- electric wall ($E_t = 0$) for the XY plane: this is done to obtain the TM modes only

- magnetic wall ($H_t = 0$) (in blue in figure 4.1) for the XZ plane: to obtain only the horizontal polarization of the modes
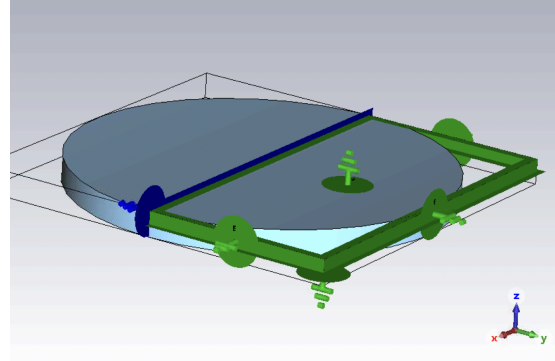
Figure 4.1: Boundary conditions definition on CST for the cavity geometry.

Conventionally, the mesh is defined to be tetrahedral for the eigenmode solver. The eigenmode solver on CST gives as results for the resonance frequencies:

$$f_{010} = 1.01543 \pm 3 \times 10^{-8} \text{ GHz} \quad \text{and} \quad f_{110} = 1.61793 \pm 1 \times 10^{-11} \text{ GHz}$$
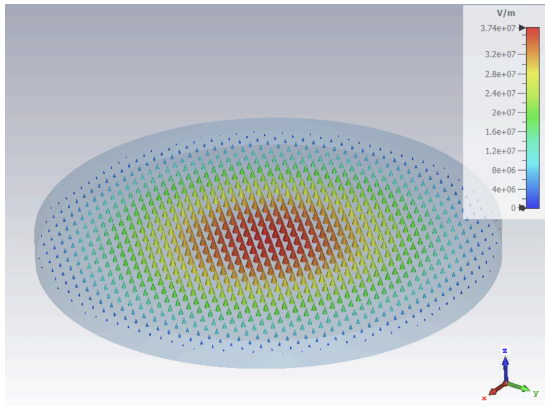
(a) Monopole mode
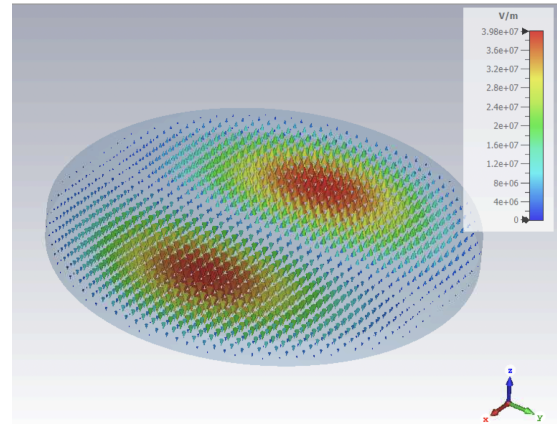
(b) Dipole mode

Figure 4.2: E-field distribution on the cavity geometry computed with CST.

Numerical frequency errors are given by CST. These preliminary results show the precision of the software and allow to verify the analytical calculation of the resonance frequencies.

Beam Pipe inclusion

Since the cavity geometry is intersected by the beam pipe, the full geometry has to be considered. The resonance frequencies are prone to change due to the "hole" in the cavity. CST is now used to numerically compute those frequencies that will be in practice the operational frequencies of the cavity. To simulate the pipe, the geometry is then modified by including a cylinder of radius

$R_p = 39$ mm (according to the ILC parameters) and a length $L_p = 200$ mm (long enough to not influence the results). The material and boundary conditions are defined exactly the same way as before. CST gives as results:

$$f_{010} = 1.122857 \pm 9 \times 10^{-7} \text{ GHz} \quad \text{and} \quad f_{110} = 1.494874 \pm 3 \times 10^{-9} \text{ GHz}$$

(a) Monopole mode　　　　　　　　　　　　　(b) Dipole mode
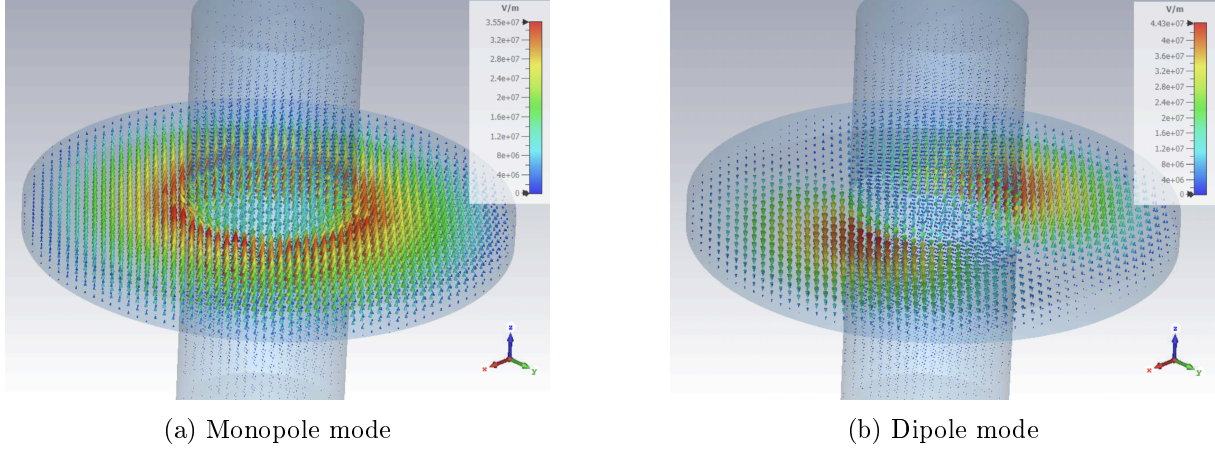
Figure 4.3: E-field distribution on the cavity geometry with the beam pipe computed with CST.

It is noticeable that the inclusion of the pipe brings the values of the two frequencies closer together. This is problematic because it makes the CM-rejection harder to achieve.

4.1.2　Dynamic range

The dynamic range of the detector is the range in which it is able to provide a valid position measurement. In this case, it corresponds to the x and y range in which the approximation $J_n(x) \simeq \frac{1}{n!} \left(\frac{x}{2} \right)^n$ for $x \approx 0$ is valid, giving equations 2.14 and 2.17. In other words, the dynamic range corresponds to the range for which the E-field along the x and y-axis can be approximated to a linear function (for the dipole mode) and can be approximated to a constant (for the monopole mode).

In figure 4.4, the E_z-field along the x-axis, extracted from the E-field distribution at $y = 0$ and $z = 0$ obtained with CST, is depicted.

(a) Dipole mode　　　　　　　　　　　　　　(b) Monopole mode

Figure 4.4: E_z-field along the x-axis for the cavity geometry with and without the beam pipe.

One can notice that there is indeed a linearity of $E_z(x)$ for the dipole mode with or without the pipe. This linearity can be approximated to be on the range $x = \pm 22$ mm. As discussed

before, the output dipole signal is normalized by the monopole signal assuming the latter is constant. One can approximate that this signal is constant again on the range $x = \pm 22$ mm from the result including the beam pipe.
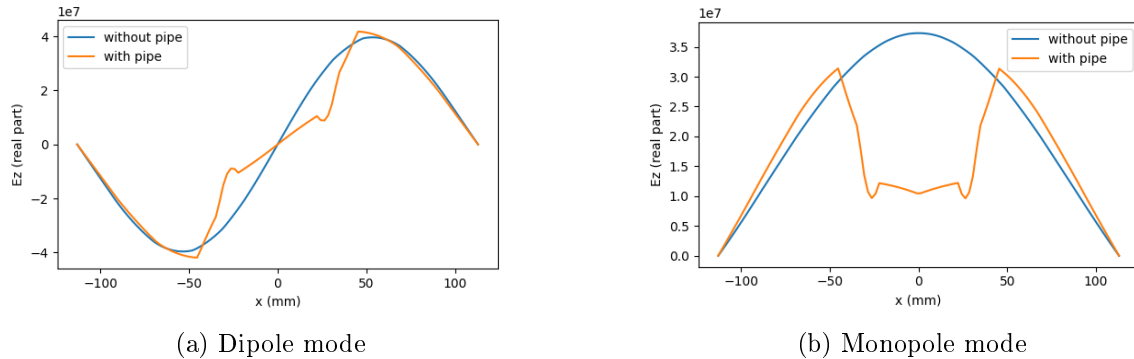
The same calculation can be performed on the y-axis observing the vertical polarization of the dipole. The result is the same due to the symmetry of the geometry.
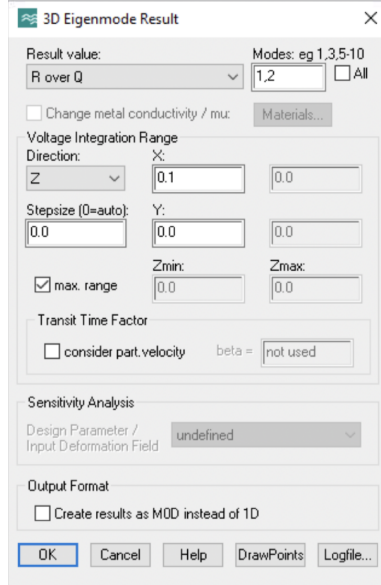
4.1.3   (R/Q) behavior

Figure 4.5: CST configuration to compute (R/Q).

When defining the cavity BPM parameters, it was shown that the normalized shunt impedance (R/Q) is linear to the beam offset squared $(\delta x)^2$ for the dipole mode (eq. 2.14), and constant for the monopole mode (eq. 2.17). To corroborate this, the post-processing tools of CST Studio allow computing (R/Q) by integrating the E_z-field along a direction at a specific position, for the monopole and dipole modes. From the definition of the shunt impedance, the integration is performed along the z direction. The coordinate y is kept constant, equal to zero, and (R/Q) is evaluated along a range of values of x coordinates:

$$x = (0.0,\ 0.1,\ 0.2,\ ...,\ 1.0)\ \text{mm}$$

The output voltage is obtained from $\sqrt{(R/Q)}$ (equation 2.22). Then, by taking the CST results of normalized shunt impedance presented before, one can compute $\sqrt{(R/Q)}$ as a function of x. This confirms:

- the linearity of the output signal for the dipole mode

- that the output signal is constant for the monopole modes.

Additionally, the results extracted from CST can be contrasted with the theoretical expressions of (R/Q). Expressions 2.14 and 2.17:

$$\left[\frac{R}{Q}\right]_{110} \simeq \frac{2\,(j_{11}\delta x)^2\,LT_r^2}{\omega_{110}\pi\varepsilon_0 a^4 J_0\,(j_{11})^2} \quad \text{and} \quad \left[\frac{R}{Q}\right]_{010} \simeq \frac{2LT_r^2}{\omega_{010}\pi\varepsilon_0 a^2 J_1\,(j_{01})^2}$$

are computed on Python (B.2) along with the CST results, by using:

- $a = 113$ mm and $L = 15$ mm

- $j_{11} \simeq 3.8317$ and $j_{01} \simeq 2.4048$, the first zeros of Bessel functions J_1 and J_0

- $w_{110} \simeq 2\pi \times 1.494874$ GHz and $w_{010} \simeq 2\pi \times 1.122857$ GHz, according to the CST results

- ε_0 the vacuum permittivity.

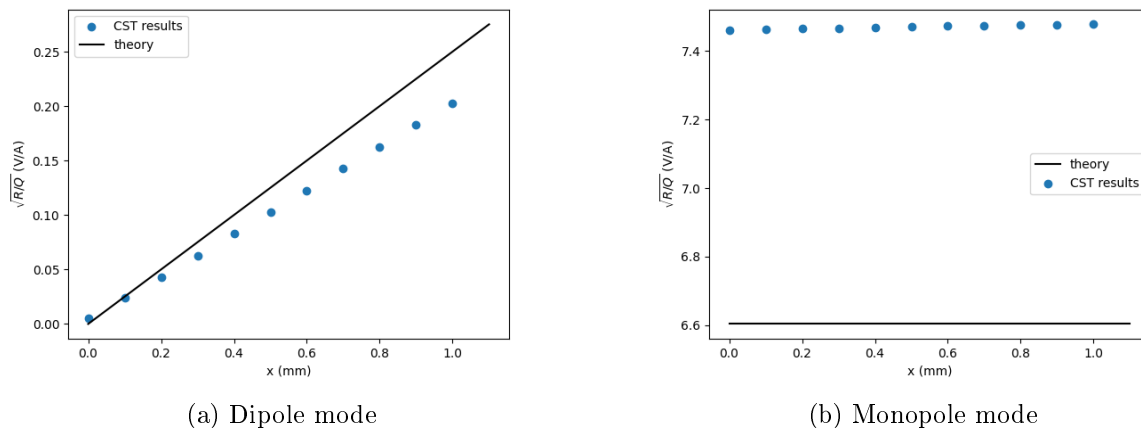(a) Dipole mode   (b) Monopole mode

Figure 4.6: $\sqrt{(R/Q)}$ along the x-axis for the cavity geometry with the pipe.

Results in figure 4.6, corroborate the linearity of $\sqrt{(R/Q)}$ for the dipole mode, and the constant behavior for the monopole mode. However, there is a discrepancy on the comparison with the theory. This can be explained by the fact that the theoretical expressions consider a closed resonant cavity without the pipe. Since the (R/Q) calculations from CST were performed on the geometry including the pipe, one can find again the differences spotted previously on figure 4.4.

4.2   Comparison of Wakefield and PIC solvers

The *wakefield* and *PIC solvers* have a different dynamic than the *eigenmode solver* presented previously. The eigenmode solver simply solves the allowed EM modes inside a geometry by solving the Maxwell Equations with certain boundary conditions. The wakefield and solver compute the interactions between an EM source and its surroundings [Com19a]. This is done by computing the fields created by a charged bunch travelling though a geometry. The PIC solver is implemented for the design of EM components used for the acceleration and guidance of charged beams. This solver provides a transient simulation by evaluating the space charge and the relativistic effects of particles propagating though high frequency EM fields [Glo].

These solvers have suitable tools for an electron beam simulation. Their performance with regard to the cavity BPM case are compared by first, analyzing their particle beam definition, and then by the identification of the dipole signal in the case of an offset beam.

4.2.1   Setup comparison: definition of the beam

For the simulation, the geometry presented before for the eigenmode study is reproduced. Then, for each of the solvers one can define a particle source differently. Figure 4.7 shows that both solvers allow the definition of a particle beam with a Gaussian shape, a charge $q = 3.2$ nC and a standard deviation $\sigma_z = 300$ μm. The wakefield solver defines a transmission line where the beam passes, whereas the PIC solver defines the beam from a source point. In general the PIC solver requires more information and is more precise on the beam definition. Other parameters such as the number of bunches, the distance between them and the beam energy can be specified.

(a) Wakefield solver   (b) PIC solver
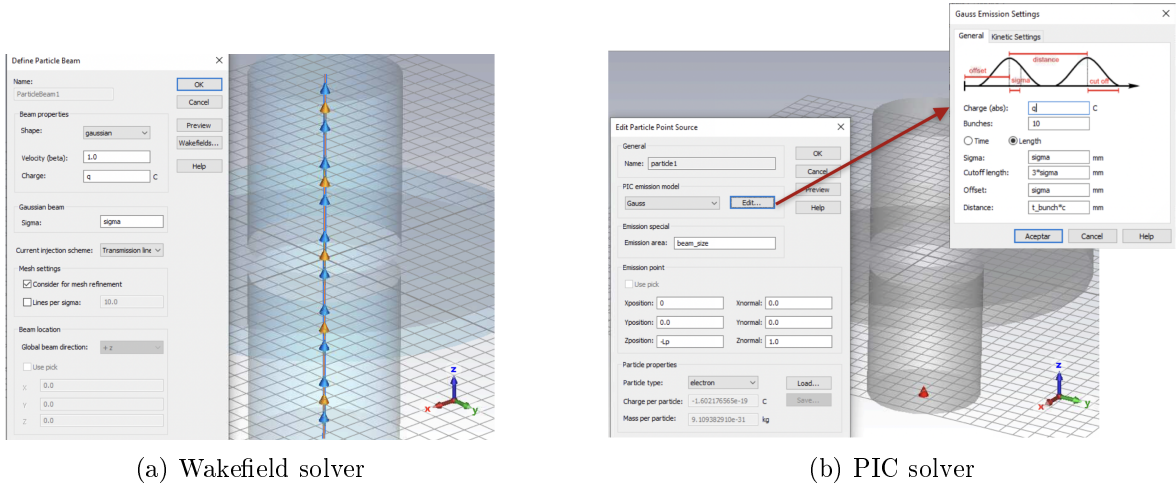
Figure 4.7: Definition of the particle beam comparison for both solvers.

The definition of the mesh in these case is hexagonal. Its size is extremely narrow since it considers the size of the bunch on the mesh definition: $\sigma_z = 300~\mu$m.

4.2.2   Identification of the dipole signal

In order to identify the dipole signal, an E-field probe is placed inside the cavity, to collect the field produced by the beam. It is placed at coordinates $(a/2, 0, 0)$. The signal collected by the E-probe is the electric field as a function of time, at the point where the probe is placed. The different modes existing in the cavity can be identified by performing a FT of the signal. Since the resonance frequency of every mode is known, they can be identified in the frequency domain. Simulations are run first by placing a beam completely centered on the pipe, and then with an offset beam with coordinates $(0.5, 0, 0)$ mm. By comparing both results one can identify the apparition of the dipole signal when the beam has an offset on the x-axis.
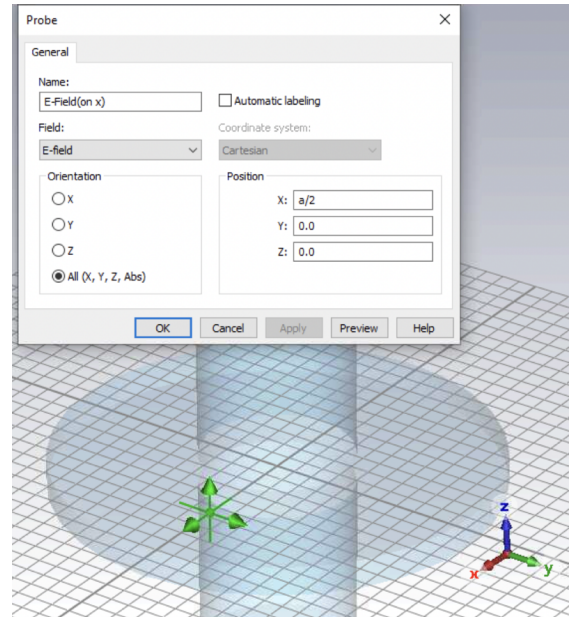
Figure 4.8: CST configuration of the E-probe.

Wakefield solver

The wakefield simulation is performed so that CST provides a result over 40 ns. The E_z field as a function of time is retrieved and processed by an in-house developed Python code (B.3), to obtain the result in the frequency domain.

Figure 4.9 shows the FT for the centered and offset beam. Both results present a large peak around 1.127 GHz, corresponding to the monopole mode signal. One can distinguish a small peak at 1.519 GHz, corresponding to the dipole mode, for the case of the offset beam. Yet, the dipole mode is barely perceivable. This can be improved by increasing the simulation time. However, because of the small bunch size and the narrow mesh implemented, this requires very large calculation times on CST.

(a) Centered beam ($\delta x = 0$ mm) (b) Offset beam ($\delta x = 0.5$ mm)
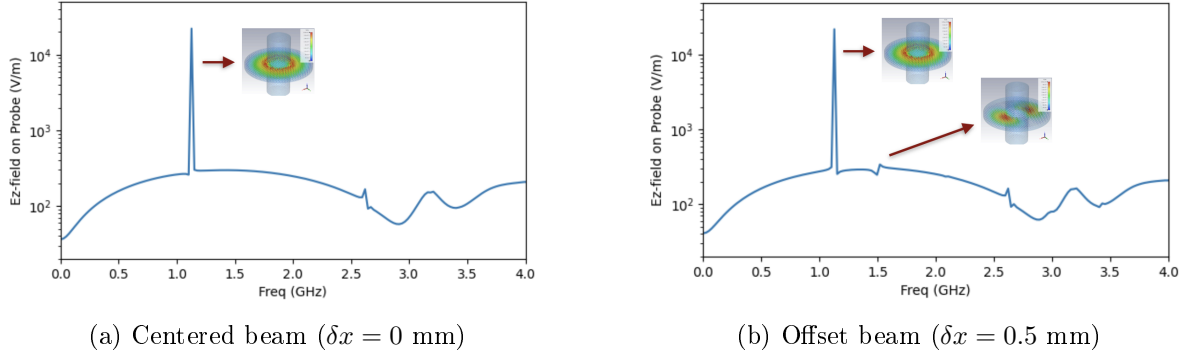
Figure 4.9: FT of the CST result from the E-probe for the wakefield solver.

PIC solver

The PIC solver simulation is obtained over 40 ns as well. Again, one can identify the monopole mode frequency around 1.254 GHz, and the dipole mode frequency at 1.5 GHz when there is an offset. The obtained frequencies for this solver are more consistent with the results obtained on the eigenmode study. However, it is noticeable that the spectrum presents broader frequency peaks. Nevertheless, the dipole peak is more clearly defined than for the wakefield solver, making simpler the identification of the beam offset.

(a) Centered beam ($\delta x = 0$ mm) (b) Offset beam ($\delta x = 0.5$ mm)
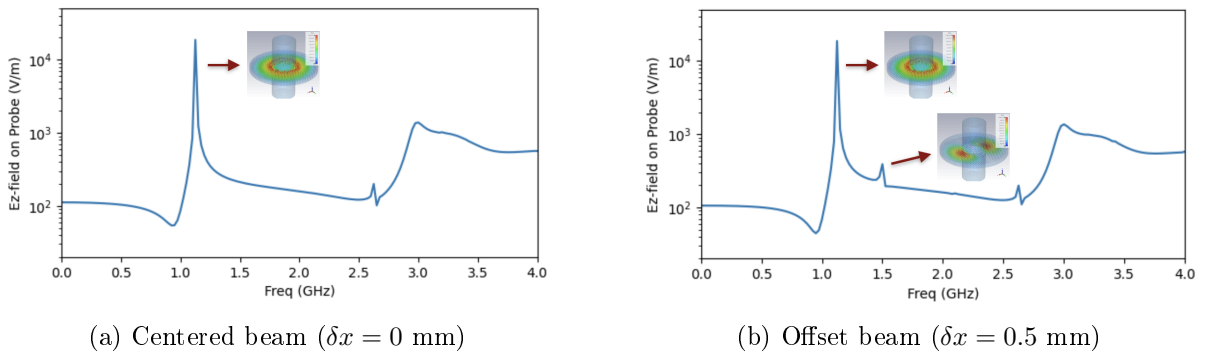
Figure 4.10: FT of the CST result from the E-probe for the PIC solver.

Overall, the PIC solver is preferred since this solver allows to make a thorough definition of the particle beam. For instance, one can specify the bunch separation t_{bunch}. This can be particularly useful when observing the detector's behavior at the passage of many bunches, since the energy inside the cavity needs to dissipate before the arrival of the next bunch.

4.3   Output results

4.3.1   Result improvement

From here on, only the PIC solver is implemented. As explained previously, because of the bunch size $\sigma_z = 300$ μm, the mesh definition is extremely narrow, which increases the calculation time considerably. It was noticed that [SW10] employed a bunch size of $\sigma_z = 24$ mm for the ILC beam-type. This bunch size was tested on CST, which allowed to decrease the simulation time substantially.

Figure 4.11 shows the result on the frequency domain obtained directly from CST. The simulation result is obtained over 300 ns. Because the simulation time is longer, one can observe that the spectrum presents more detail than the ones obtained from shorter studies. The frequency peaks are narrower, in particular for the dipole mode, which improves the position reading.

(a) Centered beam ($\delta x = 0$ mm)   (b) Offset beam ($\delta x = 0.5$ mm)
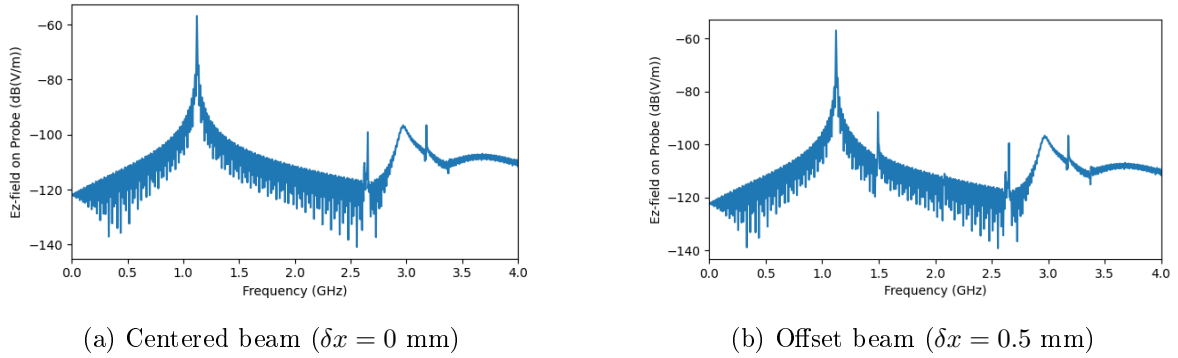
Figure 4.11: CST result from the E-probe for the PIC solver with $\sigma_z = 24$ mm.

However, it is important to recall that these results are obtained considering a PEC material for the cavity. Therefore, the losses are not taken into account. For this reason, there is almost no CM-contamination on the dipole frequency. Nevertheless, the choice of a longer bunch with $\sigma_z = 24$, gives the possibility to perform longer simulations, giving more satisfying results. It is convenient to keep using this simulation settings on further studies.

Conclusion and Discussion

Classical BPMs measure the charges induced by the beam on an insulated plate, where the strength of the signal leads to the beam position. These BPMs are however limited by their resolution and consequently, they are not suitable for the ILC project requirements. Because of their resonating behavior, cavity BPMs allow a better resolution on beam position reading (on the order of the nm). These BPMs work under the principle of excitation of special field configurations, the TM modes, by the passage of the beam through a cavity. According to the theory, a centered beam excites only the monopole modes of the cavity. The offset of a beam is identified by the generation of the dipole signal, whose amplitude is proportional to the beam displacement (until a certain range).

A proper functioning of the cavity BPM requires a careful geometry design. By choosing the cavity dimensions, one can adjust the resonance frequency of the monopole and dipole modes in such way that they are included on the frequency spectrum of the beam, and that they are evenly separated from the accelerating frequency, as suggested by the bibliography as an optimum working point based on the performance of existing designs. In the context of the ILC project, a radius of 113 mm and a length of 15 mm are shown to be optimal. This leads to operational frequencies of 1.01 GHz for the monopole mode and 1.62 GHz for the dipole mode.

An *eigenmode study* performed with CST confirms these theoretical predictions: it provides the right mode frequencies and confirms the linearity of the output signal for the dipole mode by means of an evaluation of the normalized shunt impedance behavior. Since the theory does not consider the geometry of the beam pipe, CST is used to compute the actual operational frequencies for the full geometry: 1.123 GHz for the monopole mode and 1.495 GHz for the dipole mode. The study also yields the dynamic range of the detector, ±24 mm.

Wakefield and *PIC* solvers are compared on the identification of the dipole mode signal in the case of an offset beam. Because the PIC solver allows a thorough definition of the particle beam, and since the frequency peaks are sharper, it seems to be the most suitable solver for the cavity beam study. Nevertheless, the solvers can be complementary, since the wakefield solver computes the wakepotential left by the particles after passage. It is important to evaluate this effect as well since the wakefields constitute one of the main disadvantages of the cavity BPM, because they negatively affect the performance of the accelerator.

Another issue to tackle when designing a cavity-BPM is the CM-contamination. As the maximum amplitude of the monopole mode is on the beam axis, this mode is strongly excited compared to the dipole mode. When using a lossy material for the cavity walls, the signal of the monopole mode can overlap the dipole mode signal on the frequency domain. Rectangular waveguides that only couple magnetically to the dipole mode, and with a cut-off frequency higher than the monopole mode frequency, work as very efficient high-pass filters.

A waveguide with height 122 mm is able to suppress the monopole mode field and retrieve the dipole mode signal for position reading. It may be relevant to perform a parametric simulation on the waveguide height and compute the spectral densities of both modes at f_{110}, to derive

the optimal height of the waveguide to reject the common mode, preserving the integrity of the dipole signal.

A potential area of further study would be the cavity material. The energy dissipation on the cavity must be high enough so the E-field inside the cavity disappears in between bunches, and it must be low enough so that the peaks in frequency spectrum are narrow enough to reduce the CM-contamination.

Moreover, it would be convenient to carry out studies in the resolution of the designed cavity BPM, since it is the main requirement for an accurate position monitoring for the ILC. For a detector with a proper CM-rejection the position resolution is mainly limited by the signal to thermal noise ratio. Components of the signal processing electronics can also contribute to the noise. An appropriate evaluation of the noise components would enable the calculation of the position resolution.

Finally, other geometry designs of cavity BPM remain to be studied and understood. A hybrid between a cylindrical and rectangular resonator is implemented on [SW10], leading to a very efficient CM-rejection inside the cavity itself. Additionally, re-entrant cavities are developed as well on the context of the ILC project [Sim+08] and [Luo+11]. They have a smaller system size and lower Q-value than a regular cylindrical cavity BPM.

Bibliography

[BC03]   R Bailey and Paul Collier. *Standard Filling Schemes for Various LHC Operation Modes*. Tech. rep. Geneva: CERN, 2003. URL: https://cds.cern.ch/record/691782.

[Com19a]   3DExperience Company. *CST Studio Suite Charged Particle Simulation, Workflow and Solver Overview*. 2019.

[Com19b]   3DExperience Company. *CST Studio Suite High Frequency Simulation, Workflow and Solver Overview*. 2019.

[FKL08]   Peter Forck, P. Kowina, and Dmitry Liakin. "Beam Position Monitors". In: *Synchrotron Radiation News* (2008).

[Fuj+07]   Kazuhiro Fujita et al. "Scattered-field time domain boundary element method and its application to transient electromagnetic field simulation in particle accelerator physics". In: *IEICE transactions on electronics* (2007).

[Glo]   RF Globalnet. *CST PARTICLE STUDIO Particle Dynamics Simulation*. URL: https://www.rfglobalnet.com/doc/cst-particle-studio-0001.

[Gus22]   M. Gustafsson. *Electrodynamics Lectures EITN80*. Lund University, 2022.

[Hay15]   Hitoshi Hayano. "Superconducting accelerator development at STF for ILC". In: *Proceedings of the 12th annual meeting of Particle Accelerator Society of Japan* (2015).

[Hay19]   H Hayano. "Development of L-band Cavity BPM for STF". In: *KEK* (2019).

[ILC]   ILC. *International Linear Collider*. URL: https://linearcollider.org/.

[Li+03]   Zenghai Li et al. "Cavity BPM with dipole-mode-selective coupler". In: *Proceedings of the 2003 Particle Accelerator Conference, Portland, OR, IEEE, Silver Spring, MD*. 2003.

[Lor98]   Ronald Lorenz. "Cavity Beam Position Monitors". In: *AIP Conference Proceedings* (1998).

[Luo+10]   Q Luo et al. "Cold test of S-band re-entrant cavity BPM for HLS". In: *Proc. 1st Int. Part. Accel. Conf.* 2010.

[Luo+11]   Q Luo et al. "Design and cold test of re-entrant cavity BPM for HLS". In: *Proceedings of the 2011 Particle Accelerator Conference, New York, NY, USA*. 2011, pp. 420–422.

[Nak08]   T. Nakamura. *Master Thesis: Development of BPM with high position resolution*. University of Tokyo, 2008.

[Sim+08]   Claire Simon et al. "Performance of a reentrant cavity beam position monitor". In: *Physical Review Special Topics-Accelerators and Beams* (2008).

[Smi+97]   Steven W Smith et al. *The scientist and engineer's guide to digital signal processing*. 1997.

[SW10]   Seunghwan Shin and Manfred Wendt. "Design studies for a high resolution cold cavity beam position monitor". In: *IEEE Transactions on Nuclear Science* (2010).

[Vit09]   Michele Viti. "Resonant Cavities as Beam Position Monitor". In: *Deutsches Elektronen-Synchrotron DESY* (2009).

[Wen+09]   M Wendt et al. "Status of the ILC Main Linac BPM R&D". In: *arXiv e-prints* (2009).

[Wen06]   M Wendt. "Cold Cavity BPM R&D for the ILC". In: *CARE ABI Workshop*. 2006.

[Wen11]   M Wendt. *Overview of recent trends and developments for BPM systems*. Tech. rep. Fermi National Accelerator Laboratory, 2011.

[Wen20]   M Wendt. "BPM Systems: A brief Introduction to Beam Position Monitoring". In: *arXiv e-prints* (2020).

[Wol]   Wolfram. *Bessel Function of the First Kind*. URL: https://mathworld.wolfram.com/BesselFunctionoftheFirstKind.html.

Appendix A

Electric Field on Cavities

A.1 Maxwell equations and wave equation

In electromagnetism, Maxwell equations are defined in the vacuum by Faraday's, Ampère's and Gauss's laws [Gus22]:

$$\nabla \times \boldsymbol{E}(\boldsymbol{r}, t) = -\frac{\partial \boldsymbol{B}(\boldsymbol{r}, t)}{\partial t}$$

$$\nabla \times \boldsymbol{B}(\boldsymbol{r}, t) = \mu_0 \left(\varepsilon_0 \frac{\partial \boldsymbol{E}(\boldsymbol{r}, t)}{\partial t} + \boldsymbol{J}(\boldsymbol{r}, t) \right)$$

$$\nabla \cdot \boldsymbol{E}(\boldsymbol{r}, t) = \frac{\rho(\boldsymbol{r}, t)}{\varepsilon_0}$$

$$\nabla \cdot \boldsymbol{B}(\boldsymbol{r}, t) = 0$$

with spatial coordinate $\boldsymbol{r}$, time t and nabla operator ∇. $\boldsymbol{E}$ and $\boldsymbol{B}$ are defined as the electric and magnetic fields and have units V/m and As/m^2 respectively. $\boldsymbol{J}$ is the current density, ε_0 is the permittivity of free space and μ_0 is the permeability of free space.

In vacuum, one finds the relations:

$$\boldsymbol{D}(\boldsymbol{r}, t) = \varepsilon_0 \boldsymbol{E}(\boldsymbol{r}, t) \quad \text{and } \boldsymbol{B}(\boldsymbol{r}, t) = \mu_0 \boldsymbol{H}(\boldsymbol{r}, t)$$

where $\boldsymbol{D}$ is the electric displacement and $\boldsymbol{H}$ is the magnetic field intensity.

One considers only harmonic solutions of waves trinsmitting in the z direction, so that $\boldsymbol{E} \propto e^{i(\omega t \pm k_z z)}$ and $\boldsymbol{H} \propto e^{i(\omega t \pm k_z z)}$ where $k = \omega/c_0$ is the wavenumber and ω is the angular frequency. It can be proven that each Cartesian component of $\boldsymbol{E}$ satisfies a scalar wave equation. Indeed, from Maxwell equations one can derive

$$\nabla \times (\nabla \times \boldsymbol{E}) + \varepsilon_0 \mu_0 \frac{\partial^2 \boldsymbol{E}}{\partial t^2} = \boldsymbol{0}$$

And by means of the curl of the curl identity,

$$\nabla^2 \boldsymbol{E} - \frac{1}{c_0^2} \frac{\partial^2 \boldsymbol{E}}{\partial t^2} = \boldsymbol{0} \text{ with } \nabla^2 = \frac{\partial^2}{\partial x^2} + \frac{\partial^2}{\partial y^2} + \frac{\partial^2}{\partial z^2}$$

where $c_0 = 1/\sqrt{\varepsilon_0 \mu_0}$ is the speed of light in vacuum.

Thus, the Maxwell equations in vacuum lead to the vector Helmholtz equations for E and H:

$$\begin{aligned} \nabla^2 \boldsymbol{E}(\boldsymbol{r}) + k^2 \boldsymbol{E}(\boldsymbol{r}) = \boldsymbol{0} \\ \nabla^2 \boldsymbol{H}(\boldsymbol{r}) + k^2 \boldsymbol{H}(\boldsymbol{r}) = \boldsymbol{0} \end{aligned} \tag{A.1}$$

A.2   Boundary conditions and modes

One can consider a hollow waveguide along the z-axis with surface S and with vector normal to the surface $\hat{\boldsymbol{n}}$ [Gus22]. The EM fields can be decomposed into transverse and longitudinal vectors as

$$\boldsymbol{E}(\boldsymbol{r}) = \boldsymbol{E}_{\mathrm{T}}(\boldsymbol{r}) + \hat{\boldsymbol{z}}E_z(\boldsymbol{r})$$

$$\boldsymbol{H}(\boldsymbol{r}) = \boldsymbol{H}_{\mathrm{T}}(\boldsymbol{r}) + \hat{\boldsymbol{z}}H_z(\boldsymbol{r})$$

The boundary conditions are sufficient to determining the waves that can exist inside the waveguide. For the perfectly conducting surface S, the boundary conditions can be reduced to

$$\begin{cases} \hat{\boldsymbol{n}} \times \boldsymbol{E}(\boldsymbol{r}) = \boldsymbol{0} \\ \hat{\boldsymbol{n}} \cdot \boldsymbol{H}(\boldsymbol{r}) = 0 \end{cases} \quad \boldsymbol{r} \text{ on } S \quad \Rightarrow \quad \begin{cases} E_z(\boldsymbol{r}) = 0 \\ \frac{\partial H_z(\boldsymbol{r})}{\partial n} = 0 \end{cases} \quad \boldsymbol{r} \text{ on } S \tag{A.2}$$

where $\frac{\partial H_z(\boldsymbol{r})}{\partial n} = \hat{\boldsymbol{n}} \cdot \nabla_T H_z(\boldsymbol{r})$.

One can separate E_z and H_z on the previous conditions (equation A.2), along with the Helmholtz equations (A.1). Then, one considers two cases:

- the transverse magnetic (TM) case, where the magnetic field has no z component
- the transverse electric (TE) case, where the electric field has no z component

Solutions in the two cases do not couple since there is no coupling via the boundary conditions or the differential equations. The conditions can be summarized as

$$\begin{cases} \nabla^2 E_z(\boldsymbol{r}) + k^2 E_z(\boldsymbol{r}) = 0 \\ E_z(\boldsymbol{r}) = 0 \quad \boldsymbol{r} \text{ on } S \end{cases} \quad \text{(TM-case)}$$
$$\begin{cases} \nabla^2 H_z(\boldsymbol{r}) + k^2 H_z(\boldsymbol{r}) = 0 \\ \frac{\partial H_z}{\partial n}(\boldsymbol{r}) = 0 \quad \boldsymbol{r} \text{ on } S \end{cases} \quad \text{(TE-case)} \tag{A.3}$$

Longitudinal components of the fields are of interest. One can define $E_z(\boldsymbol{r}) = v(\boldsymbol{\rho})e^{\mathrm{i}k_z z}$ and $H_z(\boldsymbol{r}) = w(\boldsymbol{\rho})e^{\mathrm{i}k_z z}$ where $\boldsymbol{\rho} = \hat{\boldsymbol{x}} + \hat{\boldsymbol{y}}$ and where $v(\boldsymbol{\rho})$ and $w(\boldsymbol{\rho})$ are always real. Thus, one can identify two eigenvalue problems for the hollow waveguide

$$\begin{cases} \nabla_{\mathrm{T}}^2 v(\boldsymbol{\rho}) + k_t^2 v(\boldsymbol{\rho}) = 0 \\ v(\boldsymbol{\rho}) = 0 \end{cases} \quad \text{(TM-case)} \quad \text{and} \quad \begin{cases} \nabla_{\mathrm{T}}^2 w(\boldsymbol{\rho}) + k_t^2 w(\boldsymbol{\rho}) = 0 \\ \frac{\partial w}{\partial n}(\boldsymbol{\rho}) = 0 \end{cases} \quad \text{(TE-case)} \tag{A.4}$$

There are non-trivial solutions v and w for discrete values of k_t^2 where $k_t^2 = k^2 - k_z^2$.

A.3   Waveguides with circular cross-section

Let's consider a circular waveguide with geometry depicted in figure A.1. For the TM mode, one can reformulate the problem in equation A.4 in polar coordinates. For the TM mode

$$\begin{cases} \nabla_{\mathrm{T}}^2 v(\boldsymbol{\rho}) + k_t^2 v(\boldsymbol{\rho}) = \frac{1}{\rho}\frac{\partial}{\partial \rho}\left(\rho\frac{\partial v(\boldsymbol{\rho})}{\partial \rho}\right) + \frac{1}{\rho^2}\frac{\partial^2 v(\boldsymbol{\rho})}{\partial \phi^2} + k_t^2 v(\boldsymbol{\rho}) = 0 \\ v(a, \phi) = 0 \end{cases}$$

And for the TE mode

$$\begin{cases} \nabla_{\mathrm{T}}^2 w(\boldsymbol{\rho}) + k_t^2 w(\boldsymbol{\rho}) = \frac{1}{\rho}\frac{\partial}{\partial \rho}\left(\rho\frac{\partial w(\boldsymbol{\rho})}{\partial \rho}\right) + \frac{1}{\rho^2}\frac{\partial^2 w(\boldsymbol{\rho})}{\partial \phi^2} + k_t^2 w(\boldsymbol{\rho}) = 0 \\ \frac{\partial w}{\partial n}(a, \phi) = 0 \end{cases}$$
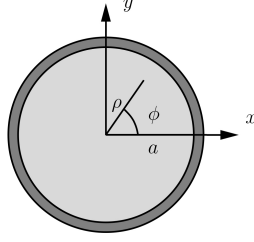
Figure A.1: Geometry of a waveguide with circular cross-section [Gus22].

By inducing $v(\rho, \phi) = F(\rho)G(\phi)$, one can use the separation of variables method, which leads to

$$\frac{\rho}{F(\rho)}\frac{\partial}{\partial\rho}\left(\rho\frac{\partial F(\rho)}{\partial\rho}\right) + k_t^2\rho^2 = -\frac{1}{G(\phi)}\frac{\partial^2 G\left(\partial\phi^2\right)}{\phi}$$

Since the right side depends only on ϕ and the left hand only on ρ, then both have to equal a constant, here denoted C. This leads to the differential equations

$$\begin{cases} \rho\frac{\partial}{\partial\rho}\left(\rho\frac{\partial F(\rho)}{\partial\rho}\right) + \left(k_t^2\rho^2 - C\right)F(\rho) = 0 \\ \frac{\partial^2 G(\phi)}{\partial\phi^2} + CG(\phi) = 0 \end{cases}$$

The solution to the eigenvalue problem for the azimuthal part $G(\phi)$ (with condition $G(\phi) = G(\phi + 2\pi)$) is

$$G(\phi) = A_m\cos(m\phi) + B_m\sin(m\phi), \quad C = m^2, \quad m = 0, 1, 2, \ldots$$

The solution to the equation for the radial dependence with boundary conditions $F(a) = 0$ and $|F(0)| < \infty$, is

$$F(\rho) = J_m(k_t\rho)$$

where J_m is the Bessel function of order m. Thus, the TM eigenvalues are given by $J_m(k_t a) = 0$ for $m = 0, 1, 2, \ldots$, which gives

$$k_{t,mn} = \frac{j_{mn}}{a} \quad \text{and} \quad k_{z,mn} = \sqrt{k^2 - k_{t,mn}^2} \tag{A.5}$$

where j_{mn} is the n-th zero of the m-th Bessel function J_m.

Similarly, it can be shown that the eigenvalues of the TE modes are given by $J_m'(k_t a) = 0$ for $m = 0, 1, 2, \ldots$, which gives

$$k_{t,mn} = \frac{\eta_{mn}}{a} \quad \text{and} \quad k_{z,mn} = \sqrt{k^2 - k_{t,mn}^2} \tag{A.6}$$

where η_{mn} is the n-th zero of the derivative of the m-th Bessel function J_m'.

It can be shown that the normalized eigenfunctions are

$$\begin{cases} v_{mn} = \frac{\sqrt{\varepsilon_m}J_m(\xi_{mn}\rho/a)}{\sqrt{\pi}aJ_m'(\xi_{mn})}\begin{pmatrix}\cos m\phi \\ \sin m\phi\end{pmatrix}, & \text{TM-case} \\ w_{mn} = \frac{\sqrt{\varepsilon_m}\eta_{mn}J_m(\eta_{mn}\rho/a)}{\sqrt{\pi(\eta_{mn}^2 - m^2)}aJ_m(\eta_{mn})}\begin{pmatrix}\cos m\phi \\ \sin m\phi\end{pmatrix}, & \text{TE-case ,} \end{cases} \tag{A.7}$$

where $\varepsilon_m = 2 - \delta_{m,0}$.

A.4   Cylindrical cavities

A finite volume of vacuum enclosed by a metallic surface constitutes a resonance cavity. One considers a cavity consisting of a hollow cylindrical waveguide terminated by metallic plane surfaces at $z = 0$ and $z = L$. This induces additional boundary conditions

$$\begin{cases} \frac{\partial E_z(x,y,0)}{\partial z} = \frac{\partial E_z(x,y,L)}{\partial z} = 0 \\ H_z(x,y,0) = H_z(x,y,L) = 0 \end{cases}$$

A mode circulating in a cylindrical cavity is the superposition of a waveguide more propagating in the positive and negative z-directions. Thus,

$$\begin{cases} E_z(\boldsymbol{r}) = \left(a_{n\nu}^+ e^{\mathrm{i}k_z z} - a_{n\nu}^- e^{-\mathrm{i}k_z z} \right) v_n(\boldsymbol{\rho}) & \nu = \mathrm{TM} \\ H_z(\boldsymbol{r}) = \left(a_{n\nu}^+ e^{\mathrm{i}k_z z} + a_{n\nu}^- e^{-\mathrm{i}k_z z} \right) w_n(\boldsymbol{\rho}) & \nu = \mathrm{TE} \end{cases}$$

Boundary conditions give $a_{n\nu}^+ = -a_{n\nu}^-$ and $\sin k_z d = 0$. Therefore k_z can only take the discrete values: $k_{z,p} = p\pi/L$ where $p = 0, 1, 2, \ldots$ for the TM modes and $p = 1, 2, \ldots$ for the TE modes. Then, frequencies that can exist inside a cylindrical cavity are

$$f_{np} = \frac{c_0}{2\pi} \sqrt{k_{t_n}^2 + \left(\frac{p\pi}{L} \right)^2}$$

In the case of a circular-cylindrical cavity, also known as *pill-box* cavity, with radius a and length L, one can derive the expressions of E_z and H_z by means of equations A.7. It is shown that the TE modes have an E_z field

$$E_{z,mnp}(\rho, \phi, z) = C_{mnp} J_m \left(\xi_{mn} \rho/a \right) \cos(m\phi) \cos \left(\frac{pz}{d} \right), m = 0, 1, \ldots, n = 1, 2 \ldots, p = 0, 1 \ldots \tag{A.8}$$

and the TE-modes have an H_z field

$$H_{z,mnp}(\rho, \phi, z) = C_{mnp} J_m \left(\eta_{mn} \rho/a \right) \cos(m\phi) \sin \left(\frac{pz}{d} \right), m = 0, 1, \ldots, n = 1, 2 \ldots, p = 1, 2 \ldots \tag{A.9}$$

where C_{mnp} is their amplitudes.

By merging this result with the one obtained for the cylindrical waveguides, one can derive that the eigenfrequencies are given by

$$f_{mnp} = \begin{cases} \frac{c_0}{2\pi} \sqrt{\left(\frac{j_{mn}}{a} \right)^2 + \left(\frac{p\pi}{L} \right)^2} & \mathrm{TM} \\ \frac{c_0}{2\pi} \sqrt{\left(\frac{\eta_{mn}}{a} \right)^2 + \left(\frac{p\pi}{L} \right)^2} & \mathrm{TE} \end{cases} \tag{A.10}$$

Appendix B

Developed Python codes

B.1 Simulation of the ILC beam signal and its FT

```python
import numpy as np
from scipy.integrate import quad
import matplotlib.pyplot as plt
from decimal import Decimal

#------------------------------------------------------------#
## Variable definition
#------------------------------------------------------------#
q_bunch = 3.2 # nC charge of a bunch
sigma_z = 300 # microm lenght of a bunch
c = 3e5 # microm/ns speed of light
t_sigma_z = sigma_z/c # ns length of a bunch in time
t_bunch = 369 # ns spacing between bunches
f_bunch = 1/t_bunch # frequency of repetition of bunches
f_rep = 5e-9 # GHz frequency of repetition of macro-pulses
t_rep = 1/f_rep # ns spacing between macro-pulses
f_RF = 1.3 #GHz frequency of RF cavities
n = t_bunch*f_RF # number of bunches
t_beam = n*t_bunch # ns lenght of a macro-pulse in time
fs = 10/t_sigma_z # sample frequency
step = 1

#------------------------------------------------------------#
## Function definition
#------------------------------------------------------------#
def i_bunch(t):
    # gaussian pulse for a single bunch
    return q_bunch/(t_sigma_z*np.sqrt(2*np.pi)) * np.exp(-(t)**2/(2*t_sigma_z
    **2))

def i_bunch_FT(f):
    # FT of the gaussian pulse for a single bunch
    return q_bunch * np.exp(-2*(t_sigma_z*np.pi*f)**2)

def train_delta1(t):
    # dirac comb pulse
    deltas = np.zeros(len(t))
    indices = np.where(t%t_bunch==0)
    deltas[indices[0]] = 1
```

```python
40          return deltas
41
42   def train_delta2_FT(f):
43          # FT of dirac comb pulse in GHZ
44          deltas = np.zeros(len(f))
45          for i in range(len(f)):
46               A = str(round(f[i],9)) # round to Hz
47               if Decimal(A)%Decimal('0.0027')==Decimal('0.0'):
48                    deltas[i]=1
49          return deltas
50
51   def rect_pulse(t):
52          #rectancular pulse for macropulse
53          res = np.zeros(len(t))
54          for k in range(0,5):
55               indices = np.where((t>k*t_rep) & (t<k*t_rep+t_beam))
56               res[indices[0]] = 1
57          return res
58
59   def rect_pulse_FT(A,d,N):
60          # FT of rectancular pulse for macropulse (synthesis equation)
61          res = []
62          for k in range(N):
63               if k==0:
64                    res.append(A*d) #a_0
65               else:
66                    a_k = 2*A/(k*np.pi)*np.sin(k*np.pi*d)
67                    res.append(abs(a_k))
68          return res
69
70   #----------------------------------------------------------#
71   ### TIME DOMAIN
72   #----------------------------------------------------------#
73   # Time definition
74   t_end = 1e4 # ns
75   time = np.arange(0,t_end,step) # time vector
76
77   # Gaussian pulse
78   t_in = -0.005
79   t_fin = 0.005
80   time_gauss = np.arange(t_in,t_fin,1e-5)
81   bunch = i_bunch(time_gauss)
82   # Check value integral:
83   charge_bunch = quad(i_bunch, t_in, t_fin)
84   print(charge_bunch)
85   plt.plot(time_gauss,bunch)
86   # plt.title('Single Bunch')
87   plt.xlabel('Time (ns)')
88   plt.ylabel('Intensity (A)')
89   plt.grid()
90   plt.show()
91
92   # Delta train 1
93   dirac_comb = train_delta1(time)
94   plt.plot(time,dirac_comb)
95   #plt.title('Dirac Comb')
96   plt.xlabel('Time (ns)')
97   plt.ylabel('Intensity (A)')
98   plt.grid()
99   plt.show()
```

```
100
101  # Rectangular pulse
102  time_rect = np.arange(0,6e5,1e3) # time vector
103  rect = rect_pulse(time_rect)
104  plt.plot(time_rect,rect)
105  #plt.title('Rectangular function')
106  plt.xlabel('Time (ns)')
107  plt.ylabel('Intensity (A)')
108  plt.grid()
109  plt.show()
110
111  #_____#
112  ### FOURIER TRANSFORMS
113  #_____#
114  # Frequency definition
115  f_end = 6e2
116  freq_delta = np.arange(0,f_end,1e-4) #  GHz ; step = 0.1 MHz
117
118  # Gaussian pulse
119  f_in = 0
120  f_fin = 8e2
121  freq_gauss = np.arange(f_in,f_fin,1e-4)
122  bunch_FT = i_bunch_FT(freq_delta)
123  plt.plot(freq_gauss,bunch_FT)
124  #plt.title('Single Bunch FT')
125  plt.xlabel('Frequency (GHz)')
126  plt.ylabel('Intensity (A)')
127  plt.grid()
128  plt.show()
129
130  # #Delta train 1
131  dirac_comb_FT = train_delta2_FT(freq_delta)
132  plt.plot(freq_delta,dirac_comb_FT)
133  # plt.title('FT of Dirac Comb')
134  plt.xlabel('Frequency (GHz)')
135  plt.ylabel('Intensity (A)')
136  plt.grid()
137  plt.show()
138
139  # Multiplication in the frequency domain
140  FT_BS_mult = dirac_comb_FT*bunch_FT
141  plt.plot(freq_delta,FT_BS_mult)
142  # plt.title('Fourier Transform of Beam signal (without rectangular pulse)')
143  plt.xlabel('Frequency (GHz)')
144  plt.ylabel('Intensity (A)')
145  plt.grid()
146  plt.show()
147
148  # Rectangular pulse
149  A = 1 # amplitude of rectangular pulse
150  d = t_beam/t_rep #variable
151  N = int(5e3) # number of harmonics
152  freq_pulse = np.linspace(0,f_rep*N,N) # has to have 5 Hz step to work
153  rect_FT = rect_pulse_FT(A,d,N)
154  plt.bar(freq_pulse,rect_FT,width=2e-9)
155  #plt.title('FT of rectangular pulse')
156  plt.xlabel('Frequency (GHz)')
157  plt.ylabel('Intensity (A)')
158  plt.grid()
159  plt.show()
```

B.2   (R/Q) calculation and comparison with CST results

```python
import numpy as np
import matplotlib.pyplot as plt
from numpy import loadtxt
from scipy.special import jv

## Read R/Q as a function of x coordinate for CST results
file_name = "data_CST/eigenmode_study/R-Q_TM010_TM110.txt"
data = loadtxt(file_name, comments="#", delimiter="\t", unpack=False)
modes = data[:,0]
R_Q = data[:,1]
# Monopole mode
R_Q_010 = np.copy(R_Q)
R_Q_010[modes==2] = 0
R_Q_010 = R_Q_010[R_Q_010!=0]
# Dipole mode
R_Q_110 = np.copy(R_Q)
R_Q_110[modes==1] = 0
R_Q_110 = R_Q_110[R_Q_110!=0]

# x-coordinate
x = np.arange(0,1.1,0.1) # mm

## Theory
delta_x = np.linspace(0,1.1) # mm
# Variable definition
j11 = 3.8317
j01 = 2.4048
L = 15 # mm cavity length
a = 113 # mm cavity radius
w_110 = 2*np.pi*1.494874 # GHz
w_010 = 2*np.pi*1.122857 # GHz
c = 300 # mm/ns
Tr = (np.sin(w_110*L/(2*c)))/(w_110*L/(2*c))
ep_0 = 8.8541878128e-6 # vacuum permitivity nF/mm
J0_j11=jv(0, j11)
J1_j01=jv(1, j01)

# Dipole mode
R_Q_110_th = (2*(j11*delta_x)**2 * L * Tr**2)/(w_110*np.pi*ep_0*a**4 *J0_j11**2)
# Monopole mode
R_Q_010_th = (2* L * Tr**2)/(w_010*np.pi*ep_0*a**2 *J1_j01**2)
R_Q_010_th = np.full(np.shape(delta_x),R_Q_010_th)

## Plot
plt.figure()
plt.plot(delta_x,np.sqrt(R_Q_010_th), label='theory', color ='k')
plt.scatter(x,np.sqrt(R_Q_010), label='CST results')
plt.xlabel('x (mm)')
plt.ylabel(r'$\sqrt{R/Q}$ (V/A)')
# plt.title(r'$\sqrt{R/Q}$'+' as a function of x (monopole)')
plt.legend()
plt.show()

plt.figure()
```

```
55  plt.scatter(x,np.sqrt(R_Q_110), label='CST results')
56  plt.plot(delta_x,np.sqrt(R_Q_110_th), label='theory', color ='k')
57  plt.xlabel('x (mm)')
58  plt.ylabel(r'$\sqrt{R/Q}$ (V/A)')
59  # plt.title('Sqrt of R/Q as a function of x (dipole)')
60  plt.legend()
61  plt.show()
```

B.3   E-probe CST results and FT

```
1   import numpy as np
2   import matplotlib.pyplot as plt
3   from numpy import loadtxt
4   from scipy.fft import fft, fftfreq
5
6   ## Read and plot the signal as a function of time
7   file_name = "data_CST/pic_study/E_z(t)_pic_centered_sigma24.txt"
8   data = loadtxt(file_name, comments="#", delimiter="\t", unpack=False)
9   time = data[:,0]
10  E_probe = data[:,1]
11
12  plt.figure()
13  plt.plot(time,E_probe)
14  plt.xlabel('Time (ns)')
15  plt.ylabel('Ez-field on Probe (V/m)')
16  # plt.title('Ez-field as a function of time on probe')
17  plt.show()
18
19  ## Fourier Transform
20  N = len(time)
21  duration = time[-1] # ns
22  sample_rate = N/duration #GHz
23  normalize = N/2
24  E_probe_f = fft(E_probe)
25  freq_ft = fftfreq(N, 1 / sample_rate)
26  # Fix results
27  E_probe_f[freq_ft<0] = 0 # minimum freq
28  E_probe_f[freq_ft>10] = 0 # maximum freq
29  E_probe_f = E_probe_f[E_probe_f!=0]
30  freq_ft[freq_ft<0] = 0 # minimum freq
31  freq_ft[freq_ft>10] = 0 # maximum freq
32  freq_ft = freq_ft[freq_ft!=0]
33  freq_ft= np.append(0,freq_ft) # add the lost zero
34
35  plt.figure()
36  plt.plot(freq_ft, np.abs(E_probe_f)/normalize)
37  plt.xlabel('Freq (GHz)')
38  plt.ylabel('Ez-field on Probe (V/m)')
39  # plt.title('FFT of the Ez-field on probe')
40  plt.xlim(0,4)
41  plt.ylim(1e0,3e4)
42  plt.yscale('log')
43  plt.show()
```

Appendix C

Developed MATLAB codes

C.1   Computing the TM eigenfrequencies

```matlab
1  clc
2  clear all
3
4  global c0
5  c0 = 3e2; % speed of light [mm/ns]
6
7  a = 113; % radius of the cavity [mm]
8  L = 15; % length of the cavity [mm]
9
10 kmn_010 = wave_num(0,1,0,a,L); % wavenumber monopole [1/mm]
11 kmn_020 = wave_num(0,2,0,a,L); % wavenumber  second monopole [1/mm]
12 kmn_110 = wave_num(1,1,0,a,L); % wavenumber dipole [1/mm]
13
14 f_010 = freq(kmn_010); % eigenfrequency of the monopole [GHz]
15 f_020 = freq(kmn_020); % eigenfrequency of the second monopole [GHz]
16 f_110 = freq(kmn_110); % eigenfrequency of the dipole [GHz]
17
18 function res = freq(k)
19     % returns the resonance frequency for a wavenumber k
20     global c0
21     res = c0*k/(2*pi);
22 end
23
24 function res = wave_num(m,n,l,a,L)
25     % returns the wave number of a pillbox cavity of dimensions a and L
26     eps = eps_mn(m,n);
27     res = sqrt((eps/(a))^2 + (l*pi/L)^2);
28 end
29
30 function res = eps_mn(m,n)
31     % returns the root n of the bessel function of order m
32     eps_list = besselzero(m,5);
33     res = eps_list(n);
34 end
```